Available online at www.sciencedirect.com
SCIENCE DIRECT®
Journal of Magnetic Resonance 169 (2004) 129–163
JMR Journal of Magnetic Resonance
www.elsevier.com/locate/jmr

Comparing continuous wave progressive saturation EPR and time domain saturation recovery EPR over the entire motional range of nitroxide spin labels

Robert D. Nielsen, Stephane Canaan,[1] James A. Gladden, Michael H. Gelb, Colin Mailer,[2] and Bruce H. Robinson*

Department of Chemistry, University of Washington, Seattle, WA 98195, USA

Received 30 October 2003; revised 8 April 2004

Abstract

The measurement of spin–lattice relaxation rates from spin labels, such as nitroxides, in the presence and absence of spin relaxants provides information that is useful for determining biomolecular properties such as nucleic acid dynamics and the interaction of proteins with membranes. We compare *X*-band continuous wave (CW) and pulsed or time domain (TD) EPR methods for obtaining spin–lattice relaxation rates of spin labels across the entire range of rotational motion to which relaxation rates are sensitive. Model nitroxides and spin-labeled biological species are used to illustrate the potential complications that arise in extracting relaxation data under conditions typical to biological experiments. The effect of super hyperfine (SHF) structure is investigated for both CW and TD spectra. First and second harmonic absorption and dispersion CW spectra of the nitroxide spin label, TEMPOL, are all fit simultaneously to a model of SHF structure over a range of microwave amplitudes. The CW spectra are novel because all harmonics and microwave phases were acquired simultaneously using our homebuilt CW/TD spectrometer. The effect of the SHF structure on the pulsed free induction decay (FID) and pulsed saturation recovery spectrum is shown for both protonated and deuterated TEMPOL. We present novel pulsed saturation recovery measurements on biological molecules, including spin–lattice relaxation rates of spin-labeled proteins and spin-labeled double-stranded DNA. The impact of structure and dynamics on relaxation rates are discussed in the context of each of these examples. Collisional relaxation rates with oxygen and transition metal paramagnetic relaxants are extracted using both continuous wave and time domain methods. The extent of the errors inherent in the CW method and the advantages of pulsed methods for unambiguously measuring collisional relaxation rates are discussed. Spin–lattice relaxation rates, determined by both CW and pulsed methods, are used to determine the electrostatic potential on the surface of a protein.

Keywords: EPR; Spin labels; Nitroxides; Time domain; Progressive saturation; Spin–lattice rates

1. Introduction

The structure and dynamics of biological materials are routinely studied by EPR and the spin-label method. A combination of site-directed mutagenesis and spin labeling has become standard for EPR studies of proteins [1–3]. Site specific incorporation of spin labels into DNA and RNA has been accomplished with spin labels either rigidly incorporated or attached through a flexible linker [4–8]. Spin-labeled biological materials are generally studied with continuous wave (CW) EPR techniques such as progressive power saturation and saturation transfer EPR (ST-EPR) [9]. The power saturation method has been the approach of choice for determining collision-induced relaxation of spin-labeled proteins in environments containing spin relaxants, and has provided structural and functional information [10,11]. The CW power saturation technique analyzes

* Corresponding author. Fax: 1-206-685-8665.
E-mail address: robinson@chem.washington.edu (B.H. Robinson).
[1] Present address: AFMB-UMR6098, 31 Chemin Joseph Aiguier 13402, Marseille Cedex 20, France.
[2] Present address: University of Chicago, Chicago IL, USA.

1090-7807/$ - see front matter © 2004 Elsevier Inc. All rights reserved.
doi:10.1016/j.jmr.2004.04.010

the microwave power dependence of certain spectral features (typically the central peak-to-peak height for ^{14}N nitroxides) to extract relaxation rates. Collisonal relaxation studies rely upon accurate extraction of the increase in the spin-label relaxation rates that occurs in the presence of a relaxant species. In contrast, spin-label dynamics are typically inferred from the CW spectrum at a single (low) microwave power. Nitroxide correlation times are determined either by direct simulation of the whole CW spectrum, or from the measurement of a set of spectral parameters (features) that have been calibrated to a dynamics (correlation time) scale. If the spin label relaxation rates are quantified directly, their dependence on motion may also be used to assess dynamics [12,13].

Time domain (TD) techniques consisting of pulsed saturation recovery (pSR) and pulsed electron double resonance (pELDOR) offer alternatives to CW EPR methods for measurement of relaxation rates [14]. There has been much interest in pSR as a technique for biological applications since Huisjen and Hyde [15] made the first pSR measurement on a spin-labeled biological molecule, hemoglobin. The introduction of the loop-gap resonator (LGR) has improved both pSR and pELDOR sensitivity [16]. pSR has been applied to oxygen collisional relaxation in membranes, and has been demonstrated for other collisional relaxants in biological applications [17–19]. There is a renewed interest in using TD as a complement to CW techniques, especially for collisional relaxation studies [20,21]. The motivation for our use of TD EPR is to increase the accuracy of relaxation rate measurements, so that both the dynamic and structural dependence of the relaxation rates of spin-labeled biological samples may be used quantitatively.

It is our purpose here to compare the TD and CW techniques for the measurement of both the spin–spin and spin–lattice relaxation rates. We have a novel *X*-band TD/CW spectrometer that can perform CW experiments; CW progressive saturation, and STEPR as well as the TD techniques of FID, pSR, and pELDOR with only minor software changes from one type of experiment to the next. To illustrate the comparison over a broad range of routine EPR regimes, we have examined molecular motion from the 10-ps to the 10 μs timescales (see Section 2). A model nitroxide undergoing fast motion is studied to illustrate how relaxation rates can be obtained for a typical fast motion system. The fast motion study also underscores the importance of SHF structure for both CW and TD analysis. The spin–spin ($R_2 = 1/T_2$) and spin–lattice ($R_1 = 1/T_1$) relaxation rates of the nitroxide TEMPOL are obtained from extensive fitting of CW spectra consisting of absorption and dispersion signals at both the first and second harmonics of Zeeman modulation under both linear and saturating microwave power conditions. We show that the SHF structure has profound effects on the apparent relaxation rates measured by both CW and TD methods. We used spin-labeled proteins and DNA as examples to compare the methods for extraction of relaxation rates in the intermediate and slow motion regimes by both TD and CW EPR, and demonstrate the applicability and potential superiority of TD techniques for typical biological conditions. In particular, we compare pSR with CW progressive saturation. CW progressive saturation involves the product of spin–spin and spin–lattice relaxation rates ($R_1 \cdot R_2$), from which information is obtained through the sensitivity of the spin–lattice relaxation rate. In the intermediate motion regime, we show that the quantitative evaluation of the individual relaxation rates is compromised in the CW case, as opposed to the pSR case, because the CW-measured parameter depends on both R_1 and R_2. For slow motion we show that pSR is a viable technique, and illustrate how CW progressive saturation may be modified to obtain quantitative relaxation information. Throughout, comparison is made with model nitroxides that have been studied extensively for the motional dependence of their relaxation rates [13,22,23]. The nitroxide TEMPOL was chosen to study SHF effects because it is a commonly studied model nitroxide, and has been the subject of both CW and TD investigation [13,22,24]. CTPO was used for comparison with spin-labeled proteins, as it is structurally similar to the spin labeling moiety MTSSL (see Section 2).

2. Methods and materials

2.1. Instrumentation

We provide a brief description of the EPR spectrometer to illustrate some of the novel features of the instrument. The spectrometer is designed to allow one to perform both CW and TD EPR sequentially. The CW experiment conventionally involves modulation of the applied Zeeman field at a rate between 1 and 100 kHz. The instrument described here utilizes field modulation, but the method of detection differs from the standard lock-in detection. In a TD experiment microwave radiation is applied as a pulse and the response of the sample to the pulse is subsequently monitored. The timescale of the TD response is determined by the relaxation rates of the paramagnetic system; in the present context the relaxation times associated with aqueous nitroxides are on the order of microseconds. Therefore, a TD detection system must have sufficient bandwidth to measure microsecond transients. The bandwidth requirements for CW detection (kHz) and TD detection (100 MHz) are widely different. The spectrometer described below was constructed so that both CW and TD measurements could be done with the same instrument.

Fig. 1 shows a simplified block diagram of the spectrometer bridge. The observe microwave source (upper left) provides microwave power for the CW experiments and for the observe power in a (pSR) TD experiment. The observe source is driven from the output of a solid-state diode oscillator that is coupled into a cylindrical resonator, and follows published designs [25]. The microwave frequency is selected by adjusting the size of the cylindrical cavity with high precision stepping motors [26]. The observe power is split four ways (labeled A, B, C, and D). A portion of the observe microwave source power (through path C) is incident on the microwave resonator containing the sample G. Another path, B, serves as a reference. The output from the resonator G is amplified and meets the reference path B at the detectors F. The absorption and dispersion response of the paramagnetic sample induces phase and amplitude changes in the transmitted microwaves (leaving G) relative to incident microwaves, which are detected at F relative to the standard phase and amplitude provided by the reference (from path B). The microwaves that are incident on the resonator G, through path C, are unaltered expect for the action of a mechanical attenuator, which adjusts the power incident on the resonator (containing the sample). The reference path B contains a quadrature phase shifter. An expanded schematic of the quadrature mixer element is shown at the bottom of the figure, H. The quadrature phase shifter splits the input power into two channels; one with a 90° phase delay, and another with no phase shift (0°). The 0° and 90° channels are each in turn input into their own microwave mixers. The "IF" of each mixer is driven by an external DC signal (dotted lines in Figs. 1B and H). The external DC signal controls the amplitude and sign of the microwave radiation that is passed to the "RF" or output port of each mixer. After passing through the mixers the two outputs from the 0° or 90° channels are combined (summed) equally. The DC signals on each mixer are adjusted so that the combined output of the two channels is phase shifted in total by either 0°, 90°, 180°, or 270°. The purpose of the quadrature phase shifter is to digitally select the reference phase from these four possible choices without affecting the relative amplitude of the microwave power. This enables the spectrometer to perform CYCLOPS type data acquisition [27]. CYCLOPS cycling improves the signal-to-noise and also reduces the amount of coherent noise introduced into the signals. Because mixer operation involves loss of microwave power the reference signal is amplified after the quadrature phase shifter to restore lost power. The reference signal is then used as one of the inputs to the detector F. The other input to the detector is the amplified signal from the sample G.

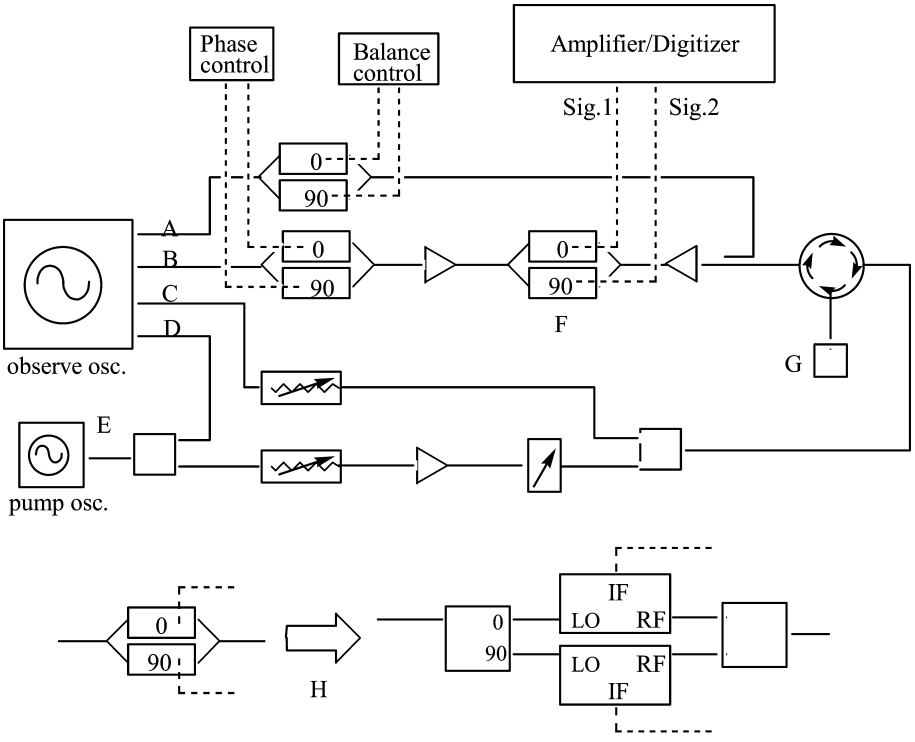

Fig. 1. Spectrometer block diagram. (A) Balance arm; (B) reference arm; (C) observe arm; (D) pump arm; (E) pump oscillator; (F) detector mixers; (G) resonant cavity; and (H) expanded schematic of mixers. Amplifiers are indicated by triangles. Attenuators are shown as variable resistors. Combiner/splitters are squares with three connections. The microwave circulator is connected to the resonant cavity G; the arrows represent the direction of microwave propagation. External connections are shown with dotted lines.

The detector F uses two microwave mixers, but in a mode of operation that is different from the reference mixers. The IF port of each mixer is the output, and is the "detected" signal. The IF ports are connected to preamplifiers and a digitizer, for data collection. The 0° channel is labeled sig.1 in Fig. 1, and the 90° channel is labeled sig.2. When the mixers are used as detectors the LO and RF signals mix and the IF output is the interference amplitude. When the RF signal contains sub-microwave modulation (as in a CW modulation experiment) the IF amplitude is modulated at the same sub-microwave frequency. If the reference quadrature phase shifter is set so that there is no phase shift, the detector mixer in the 0° channel (sig.1) gives the amplitude of the microwave signal component that is "in phase" with respect to the reference observe oscillator microwaves. The detector mixer in the 90° channel (sig.2) gives the amplitude of the microwave signal component that is "out of phase" with respect to the observe oscillator microwaves. The in phase signal is the absorption and the out of phase signal is the dispersion.

A balance arm (A) has been incorporated into the spectrometer design. The balance arm is driven from the observe oscillator, and operates analogously to the reference quadrature phase shifter. The purpose of the balance arm is to inject microwave power of arbitrary phase and amplitude into the signal leaving the resonator G. The balance power can be used to cancel the effect of microwave radiation that spuriously "reflects" off the junction to the resonator G and never interacts with the sample.

The pump path D is used when the spectrometer operates in pulsed mode. The pump oscillator E is a tunable transistor microwave source, and is a separate source of power from the observe oscillator. The pump oscillator supplies the microwave power necessary for the large amplitude microwave pulses used in a TD experiment. The observe oscillator supplies a reference signal to the pump arm (through path D) so that the frequency and phase of the pump oscillator can be set relative to the frequency and phase of the observe oscillator. The output of the pump oscillator is connected to a mechanical attenuator and an amplifier so that the amplitude of the pump pulse can be adjusted. The maximum pump power available, after amplification, is 27 dBm ($\sim$1/2 W). The output of the pump arm is blocked with a fast (nanosecond) response microwave switch. When a pump pulse is required the switch is opened and microwave power is incident on the resonator G containing the sample.

2.2. Spectrometer operation

There are several elements of spectrometer function that are common to both CW and TD operation. These include tuning of the microwave resonant cavity, adjustment of the balance bias, and adjustment of the reference phase. In order for the paramagnetic sample to interact with the microwave source the incident microwave power should be directed into the resonant cavity G, which is a loop gap resonator (LGR) designed by Hyde et al. [28,29]. The junction that connects the resonant LGR to the spectrometer has an adjustable mechanical element, which controls the coupling of the incident microwaves to the magnetic modes of the resonant cavity containing the sample. A stepper motor adjusts the coupling. In optimal operation the LGR is exactly matched to the incident power. The cavity may become de-tuned over time because of thermal heating of the resonator when the microwave power incident on the cavity is large. While the cavity may be re-tuned periodically, if automated acquisition of many TD or CW experiments is desired re-tuning becomes impractical. Therefore, a balance arm, A, was added to the spectrometer to inject microwave radiation just before the microwave amplifier and detector F. The output of the balance arm is adjusted by computer optimization of the DC IF inputs on the balance mixers (see Figs. 1A and H) so that the phase and amplitude of the balance output destructively cancels the reflection from the de-tuned cavity. Between experiments any new reflections, due to de-tuning, may be canceled by the balance arm. The Zeeman field is set off of resonance and the mixer inputs are optimized to cancel reflection from the cavity. The Zeeman field is then set back on resonance to resume the experiment. Because the balance arm is controlled digitally, this form of rebalancing is much faster and accurate than attempting to mechanically re-tune the microwave resonator between experiments.

There are two aspect of microwave phasing that are important in all experiments; (1) determination of orthogonality of the reference phase mixers, and (2) finding the absolute microwave phase. The quadrature mixers in the reference arm allow the phase of the reference microwaves to be switched digitally between 0°, 90°, 180°, and 270°. The output of each phase setting needs to be checked initially to be sure that the relative phase settings are indeed separated by intervals of 90°. In addition, the amplitude of the output of each phase setting needs to be checked to make sure that the amplitude is invariant to phase setting. To do this, the resonant cavity is de-tuned mechanically, and the resulting reflection is used to systematically measure the phase settings at the detector. The DC inputs on the reference mixers are then adjusted by computer optimization to fit the desired target. If the two mixers, which make up the detector, were perfectly identical then the target would be four equally spaced points on a circle in a polar representation of the microwave phase and amplitude. The non-ideality of the detector mixers is taken into account by using an adjusted target function that accounts for the non-ideality of the detector mixers.

This target function was established by pre-calibration of the detector mixers and shows small amplitude and phase deviation from orthogonality. When the reference mixers are calibrated in this manner, the relative phase settings are separated by 90°. Microwaves that are reflected from the resonant cavity junction in this method establish the 0° reference phase setting. If the effective path length of the microwaves in the observe arm C changes, then the absolute phase must be re-adjusted. The effective path length can change as a function of the attenuator setting in path C because the attenuator has an associated phase delay that is dependent on the mechanical setting. Therefore, it is advantageous to have an experimental measure of the final microwave phase if the reference phase is not adjusted at each observe attenuator setting. It is possible to determine the absolute microwave phase from a standard CW EPR spectrum.

2.3. CW EPR detection

In a CW experiment the cavity is tuned, the reference phases are set, and any reflection from the cavity is suppressed with the balance arm as described above. The CW experiment uses the observe path C. The pump path D is inactive during a CW experiment. The attenuator in path C passes microwave power from the observe oscillator so that microwaves are continuously incident upon the resonator G. The CW experiment begins at the lowest value of the applied Zeeman magnetic field, as specified by Zeeman field sweep width and Zeeman field sweep center value. The Zeeman field is incrementally increased in time steps specified by the total sweep time. At each Zeeman field point, a modulation field is applied. The modulation frequency is typically set in the range between 1 and 100 kHz. The 0° and 90° CW signals are the IF outputs on the 0° and 90° detector mixers (sig.1 and sig.2). The signal outputs are separately amplified and digitized for several periods of the modulation frequency at a rate of 4 MHz. The amplification step contains a 1 MHz low pass filter to prevent high frequency alias at the digitization rate, and a selectable 1,10,100, or 1000 Hz high pass filter, for low frequency noise reduction. The 4 MHz sampling rate of the digitizer ensures that the Nyquist criterion is satisfied for the range of modulation frequencies used. The transient digitizer memory for each signal is 64K points, so that multiple periods of kHz modulation can be acquired. Four digitization records are obtained for each Zeeman field point, one for each of the reference phase conditions 0°, 90°, 180°, and 270° (see above). The phase averaging procedure is a variant of the CYCLOPS phase cycling method used in NMR [27]. The digitized absorption and dispersion records are numerically Fourier transformed to obtain the coefficients of the first and second harmonics of the fundamental modulation frequency. The first and second harmonic absorption and dispersion amplitudes are stored for each field increment of the Zeeman field sweep. The first harmonic absorption and dispersion amplitudes, when plotted as a function of field, constitute the standard CW EPR absorption and dispersion spectra.

2.4. TD EPR detection

A time domain experiment typically follows a CW experiment, by which the LGR is tuned and reference phase calibration is set. A CW spectrum is used to ascertain the field positions of absorption features, for example the center of an absorption peak. The spectrometer is designed to acquire an FID signal, which is the most basic TD signal, a saturation recovery (SR) signal and a pulsed ELDOR signal. An FID spectrum is acquired by placing the Zeeman field on an absorption feature. The observe arm C is disabled during an FID experiment. A pulse of microwave power from the pump oscillator E is applied to the microwave resonator G by opening an electronically controlled blanking switch for tens of nanoseconds to microseconds to produce a pulse of a desired duration. The assertion signal for the blanking switch originates from hardware (the pulse programmer) that is linked to the digitization electronics. The frequency and phase of the pump microwave source is fixed to be the same as the observe microwave source in an FID experiment using a microwave mixer that is not shown in Fig. 1. Fixing the phase and frequency the pump microwaves to be the same as the observe source enables the reference B to be used at the detector F. A mechanical attenuator on the front end of the pump oscillator controls the amplitude of the pump pulse. The detector mixers, F, and pre-amplifier are blocked during the microwave pulse by a microwave switch that is also controlled by the pulse programmer (not shown in Fig. 1). The microwave detector remains blanked for a period of time after the pulse ends (the dead time), which typically lasts tens of nanoseconds. The dead time ensures that the transient reflection from the cavity junction has decayed to a level that will not saturate the detection mixers F. At the end of the dead time, the pulse programmer opens the blanking switch that protects the detector mixers and amplifier. Concurrently the digitizer is signaled to begin acquisition on both detector channels. The maximum digitization rate in TD mode is 200 MHz. Therefore, the maximum time resolution is 5 ns per time point. The bandwidth in TD mode is set by the response of post-detector amplification equipment (not shown in Fig. 1) and is 100 MHz. The 200 MHz digitization rate satisfies the Nyquist criterion. The digitizer record is saved in transient memory. Phase cycling is implemented just as in the CW mode. Four digitization records are acquired, each with a different reference phase condition. The built-in add/subtract function of the digitizer produces the phase

averaged absorption and dispersion amplitude/time records. One complete cycle of phase averaging constitutes the FID experiment. The FID experiment may be repeated indefinitely for signal averaging purposes.

Pulse saturation recovery (pSR) and double resonance (pELDOR) experiments use the same digitization electronics, phase cycling, and balance function as the FID. There are two main differences. In the FID experiment the observe arm C is not used. In pSR the observe oscillator microwave power is applied following the pump oscillator pulse. The pump pulse microwave phase and frequency are identical to the observe/reference microwave phase and frequency in the FID experiment. In a pSR experiment the pump and observe microwave frequencies are phase-locked to a difference. The typical pump/observe frequency offset is 100 kHz for a pSR experiment. The field/frequency condition with a 100 kHz offset is only slightly perturbed. However, when the pSR experiment is repeated thousands of times this small frequency offset has the same effect as if each pSR experiment began with a different phase between the pump and observer microwaves. Uniformly averaging over all of the different phase relationships between the pump and observe microwaves leads to cancellation of the FID-like observer-microwave-independent component of the pSR spectrum. In pulsed electron double resonance (pELDOR) the pump frequency is set to the field/frequency condition of an absorption feature that is distinct from the position of the observe field/frequency position. In this way the pump power is delivered to the sample at one frequency and the effect at the observe frequency can be monitored. The magnitude of frequency offset used in a pELDOR experiment is limited by the ability of the resonant cavity to support frequencies that differ from the natural resonance frequency of the cavity. For example, if the pump frequency differs from the tuned frequency of the LGR by 30 MHz the microwave amplitude established in the resonator (that interacts with the sample) is half the value that would be obtained at the natural frequency of the resonator. A 30 MHz frequency difference corresponds to approximately 10 Gauss in field separation.

pSR and pELDOR are typically acquired in blocks of 40K acquisitions. After each block of 40K the static magnetic field is set off resonance by ~100 Gauss. Another 40K block is acquired and subtracted from the on resonance signal. This background subtraction procedure further minimizes coherent noise, and transient pump effects. In practice the microwave resonator becomes de-tuned to a noticeable level on the timescale of 10 min of repeated acquisition. The balance arm function is used periodically to cancel spurious reflections in between pSR experiments.

The instrumental parameters used in a representative pSR spectrum acquisition are: pulse length, 170 ns; pulse power, 20 dBm; dead time, 90 ns; observe power, −12 dBm; pump/observe frequency offset, +100 kHz; data points, 4096; time resolution, 5 ns/point; and scans, 4.8M (2.4M on resonance/2.4M off resonance, background). Back ground subtraction field offset: 100 Gauss, Rebalance: every 80K scans. Acquisition time: ~40 min.

2.5. Summary of instrumentation

Several aspects of the EPR spectrometer described here are novel. Both CW and TD experiments are acquired with the same data signal processing electronics. CW signals are obtained by digitizing the modulated signal in "real time." This produces a set of modulation records that last several modulation periods, and contain the complete EPR response to the modulation. The CW first and second harmonic amplitudes are obtained from the modulation records by the numerical Fourier transform. This replaces the lock-in detector used in conventional EPR spectrometers. The lock-in detector filters the analog microwave signal by frequency mixing with an analog source that has the pure spectral frequency of the desired harmonic [30]. This specialized piece of electronics is eliminated in the current design. Furthermore, the first and second harmonic signals are obtained simultaneously. Shimoyama et al. [32] and Sasaki et al. [31] have demonstrated digital detection of CW EPR by grafting a digital modulation/demodulation unit onto commercial CW spectrometers. We utilize digital CW acquisition so that the same digital electronics can be used for both CW and TD experiments. The two-channel (simultaneous absorption and dispersion) capability of the spectrometer described here is also unique. Most spectrometers only acquire a signal of a single reference phase in one experiment. A notable exception is the TD spectrometer designed by Hyde et al. [33] which uses the approach of time-locked subsampling (TLSS) to obtain simultaneous microwave phase records. The use of CYCLOPS phase averaging (common to NMR) is also a novel development, and relies upon the two-channel capacity of our instrument. Finally, the use of a balance arm to minimize reflections from the cavity junction is non-standard. In conventional spectrometers the frequency of the observe oscillator is maintained by an external feedback loop (the AFC), and so frequency drift of observe oscillator is not a source of de-tuning. No AFC was used in our spectrometer due to the exceptional stability of the observe microwave source.

2.6. Samples

$^{14}NH_{18}$ TEMPOL (4-hydroxy-2,2,6,6-tetramethylpiperidine 1-oxyl) and $^{14}ND_{17}H$ TEMPOL (MSD Isotopes) were 0.25 mM in aqueous solution buffered at pH 8.0 with 50 mM Tris–HCl.

$^{14}ND_{13}$ CTPO (2,2,5,5-tetramethylpyrrolin-1-^{14}N-1-oxyl-3-carboxamid) (CDN, Isotopes, Canada) was 0.1 mM in 85 or 100% glycerol by volume.

Expression and spin labeling of the hGIIA $sPLA_2$ (human group IIa secreted phospholipase A_2) enzyme with MTSSL (1-oxyl-2,2,5,5,-tetramethylpyrroline-3-methyl methanethiosulfonate Spin Label) has been described previously [34]. Protein concentrations were 40–50 μM with 50 mM Tris–HCl, pH 8.0, and 0.5 mM $CaCl_2$. Large unilamellar vesicles (LUV) of 25 mM DTPM (1,2-ditetradecyl phosphatidylmethanol), and 12.6 mM DTPM/126 mM Triton X-100 mixed micelles were used, as described elsewhere [34].

Chromium(III)oxalate (CROX) and nickel(ethylenediaminediacetic acid) (NiEDDA) were prepared as described elsewhere [34].

^{15}N nitroxide relaxants used were: 1 mM TEMPAMINE (2,2,6,6-tetramethylpiperidine-1-oxyl-4-amine), 1 mM TEMPOL (2,2,6,6-tetramethylpiperidine-1-oxyl-4-ol) or 1 mM Carboxy-CTPO (3-Carboxy-2,2,5,5-tetramethylpyrrolidinyl-oxyl) (gift from Dr. A. Beth, Vanderbilt University).

Spin-labeled duplex DNA samples (28-mer and 50-mer sequences) [35] were 0.1 mM in 0 or 50% sucrose with PNE buffer (10 mM sodium phosphate, pH 7, 0.1 mM EDTA, and 0.1 mM NaCl).

2.7. Theory and fitting

Fitting of the CW data for the TEMPOL nitroxide studied here utilized simultaneously the absorption and dispersion, in-phase and out-of-phase (quadrature) signals at both the first and second harmonics of the Zeeman modulation both in the linear and saturating regimes of microwave power. The fast motion form of the continued fraction formalism originally developed for simulation of saturation transfer spectra was implemented in a global analysis environment [36,37]. Global analysis allowed for simultaneous fitting of all CW signals at multiple microwave powers. The SHF structure was accounted for by convolving a single resonance condition simulation with an SHF "stick" pattern. The SHF pattern was developed by sequentially convolving each set of nuclear resonances with the previous ones, using a constant field grid. When a splitting did not fall exactly on one of the field points of the grid then the intensity of that splitting was linearly apportioned to the two grid points on either side of the splitting. Common variables including the SHF splittings, intrinsic spin–lattice and spin–spin relaxation rates, modulation frequency, and modulation amplitude were linked among data sets. Parameters individual to a cluster of data sets, for example microwave amplitude, microwave phase, and modulation phase were similarly linked within the data cluster. The fitting protocol consisted of starting with data that was phased instrumentally for absorption and dispersion and with Zeeman phase determined by the low power quadrature nulling condition [9]. The phase nulling condition for quadrature signals gives the correct phase condition to within 12° [9,38]. For the regime studied here, the quadrature signals were an order of magnitude smaller than the in-phase signals, making even a 0.5° phasing error significant. This strong dependence gave us high accuracy in the phasing of the signals. In-phase (Absorption and Dispersion) signals were fit to a model of SHF structure, and the experimental data were then iteratively Zeeman rotated (by up to ±5°) to find agreement of the quadrature signal with the theoretical predictions. Two approaches were used to scale the theory to fit to the arbitrary instrumental (voltage) amplitude. The scales for all signals were either floated independently, or were floated so as to constrain absorption and dispersion data sets to have a common scaling (at each microwave amplitude). Because only one set of conditions, i.e., absorption first harmonic in-phase, is acquired with conventional EPR spectrometers, decoupling the scaling factors on absorption vs. dispersion, for example, allowed the fitting routine to explore results that would be obtained from fitting to the conventional subsets of data. After fitting, the scale factors were plotted, and inspected for their microwave power dependence and absorption/dispersion scaling to see whether the model function had completely accounted for the effect of saturation on the absolute signal intensity, and to see what difference, if any, was apparent with respect to absorption vs. dispersion scaling. In the fitting presented below a common microwave-power-independent scale factor was optimal, but the absorption/dispersion relative amplitude varied with the SHF models used (see Section 4). Initial values of SHF splittings, and intrinsic linewidths used to initiate fitting were estimated graphically from the low power CW spectra. The number of participating SHF protons were increased sequentially, to see the effect of including each set of SHF atoms. Two representative models of SHF structure are presented below. The matrix continued fraction (see reference) that underlies the simulation routine was tested out to the 50th convergent, but the 3rd convergent was generally sufficient, as the experimental Zeeman frequency and amplitude were small [37].

Simulation of time domain pSR and FID spectra were based upon the transient response of the simple Bloch equations for the x, y, and z components of the magnetization, neglecting any nitrogen nuclear relaxation (R_{1n}) [39]. SHF structure was accounted for by assuming that the SHF lines were independent resonance conditions i.e., without any nuclear cross-relaxation process. The Bloch equations were solved in matrix form for pump period and subsequent observer period. The effect of the pump pulse was treated by assuming a pure

pump spectral frequency for the pulse duration. The Bloch equations were solved for each SHF resonance condition, as an offset from the pump frequency. As a separate alternative, the effect of the pump pulse was simulated by assuming all SHF lines were on resonance within a restricted bandwidth centered on the pump frequency during the pulse. In this approach the bandwidth of the pump frequency is determined by the pump pulse profile in the standard Fourier transform sense such that the pulse width varies inversely with the pump time. The pump/observer phase condition for saturation recovery was simulated by adding the results of 0° and 180° phase values [39].

CW progressive power saturation data, consisting of the CW first harmonic in-phase peak-to-peak height (ΔY), were fit to the equation:

$$\Delta Y = \frac{c \cdot h_1}{\left(1 + \frac{h_1^2}{P_2}\right)^{\varepsilon}}. \tag{1}$$

The microwave amplitude h_1 (in Gauss) is expressed in terms of the microwave power P (in Watts) by $h_1 = \alpha \cdot \sqrt{P}$; where α is the conversion efficiency of the resonator ($\alpha = 4$–$4.5\,\text{Gauss}/\sqrt{\text{Watt}}$ for the X-band loop gap resonator) [40,41]. The adjustable model parameters are ε and P_2. For a single homogeneous Lorentzian line $\varepsilon = 3/2$ and $P_2 = \frac{R_1 \cdot R_2}{\gamma^2}$, $\gamma = 17.6\,\text{Mrad/Gauss}$.

The effect of a collisional relaxant on the intrinsic spin-label relaxation rates was accounted for according to:

$$\begin{aligned} R_1^{\text{relaxant}} &= R_1^0 + \chi \cdot [\text{relaxant}], \\ R_2^{\text{relaxant}} &= R_2^0 + \chi \cdot [\text{relaxant}], \\ P_2^{\text{relaxant}} &= R_1^{\text{relaxant}} \cdot R_2^{\text{relaxant}}, \\ P_2^{\text{relaxant}} &= R_1^0 \cdot R_2^0 + \left(R_1^0 + \mathrm{R}_2^0\right) \cdot (\chi \cdot [\text{relaxant}]) \\ &\quad + (\chi \cdot [\text{relaxant}])^2, \\ P_2^{\text{relaxant}} &\approx P_2^0 + R_2^0 \cdot (\chi \cdot [\text{relaxant}]), \end{aligned} \tag{2}$$

where the last approximate equality holds under typical nitroxide EPR conditions $R_2 \gg R_1$ and $R_2 \gg \chi \cdot [\text{relaxant}]$. The relaxivity, χ, depends on the relative diffusion of spin-label and relaxing agent, the spin statistical exchange factor, and the collisional interaction distance [17,37]. Some authors have argued that the factor χ could be different for the R_1 and R_2 relaxation mechanisms, but under the present approximations only the χ arising from R_1 enters in the last line of Eq. (2) [42]. Measurement of R_1, P_2, and R_2 in the presence and absence of a relaxing agent (or relaxant) allows for the definition of a parameters directly proportional to the concentration of relaxant.

$$\begin{aligned} \Delta R_1 &= R_1^{\text{relaxant}} - R_1^0 = \chi \cdot [\text{relaxant}], \\ \Delta R_2 &= R_2^{\text{relaxant}} - R_2^0 = \chi \cdot [\text{relaxant}], \\ \Delta P_2 &= P_2^{\text{relaxant}} - P_2^0 \approx R_2^0 \cdot (\chi \cdot [\text{relaxant}]). \end{aligned} \tag{3}$$

Often the concentration of relaxant is the experimentally desired quantity. Controls are necessary in order to isolate the χ dependence of the change in relaxation (3). For example, in studying the binding of spin-labeled proteins to membrane substrates the effect of relaxant in the bound vs. unbound state is given by an "exposure factor," defined here for the spin–lattice relaxation rate as [10]:

$$\begin{aligned} \Phi &= \frac{\Delta R_1^{\text{membrane}}}{\Delta R_1^{\text{no membrane}}} = \frac{\chi \cdot [\text{relaxant}]_{\text{local}}^{\text{membrane}}}{\chi \cdot [\text{relaxant}]_{\text{local}}^{\text{no membrane}}} \\ &\approx \frac{[\text{relaxant}]_{\text{local}}^{\text{membrane}}}{[\text{relaxant}]_{\text{local}}^{\text{no membrane}}}. \end{aligned} \tag{4}$$

Approximate cancellation of χ factors holds when the relative diffusion of spin-label and relaxant is unaffected by binding to membranes. Analogous definitions hold for the CW P_2 parameter (see Section 3).

3. Results

3.1. H/D TEMPOL, fitting time domain and CW spectra with resolved SHF structure

The model nitroxides $^{14}NH_{18}$ TEMPOL and $^{14}ND_{17}H$ TEMPOL in deoxygenated water at 20 °C and 0.25 mM were studied by both CW and TD techniques. The CW spectra acquired consisted of eight distinct signals: absorption and dispersion at the first and second harmonics of Zeeman modulation, and the in-phase and quadrature signals. These eight signals are acquired synchronously as described in the experimental section above. CW spectra were obtained for 18 logarithmically spaced microwave amplitudes between 0.01 and 1.3 Gauss. TD spectra consisted of the FID and pulsed saturation recovery (pSR). The pulsed pump frequency was positioned on the ^{14}N center manifold, for measurements on resonance. To study off resonance effects the DC Zeeman field was adjusted incrementally so that the position of the pump traversed the SHF frequency-field resonance conditions. Pulse widths of 100–200 ns, and pump amplitudes of 1–3 Gauss were used to generate pulses between $\pi/2$ and $3\pi/2$.

Figs. 2 and 3 show the CW first harmonic and second harmonic spectra, respectively, for protonated TEMPOL at an intermediate microwave power of 0.08 Gauss, and 0.03 Gauss Zeeman modulation at 15 kHz. Only the ^{14}N center manifold is shown. Simulations of the spectra are shown as solid lines. The simulation routine including model parameters and fitting protocol are described above (see Section 2). The relaxation rates (R_1 and R_2) and SHF splittings were obtained from a simultaneous fit of all 8 signals at all 12 microwave amplitudes logarithmically spaced between 0.015 and

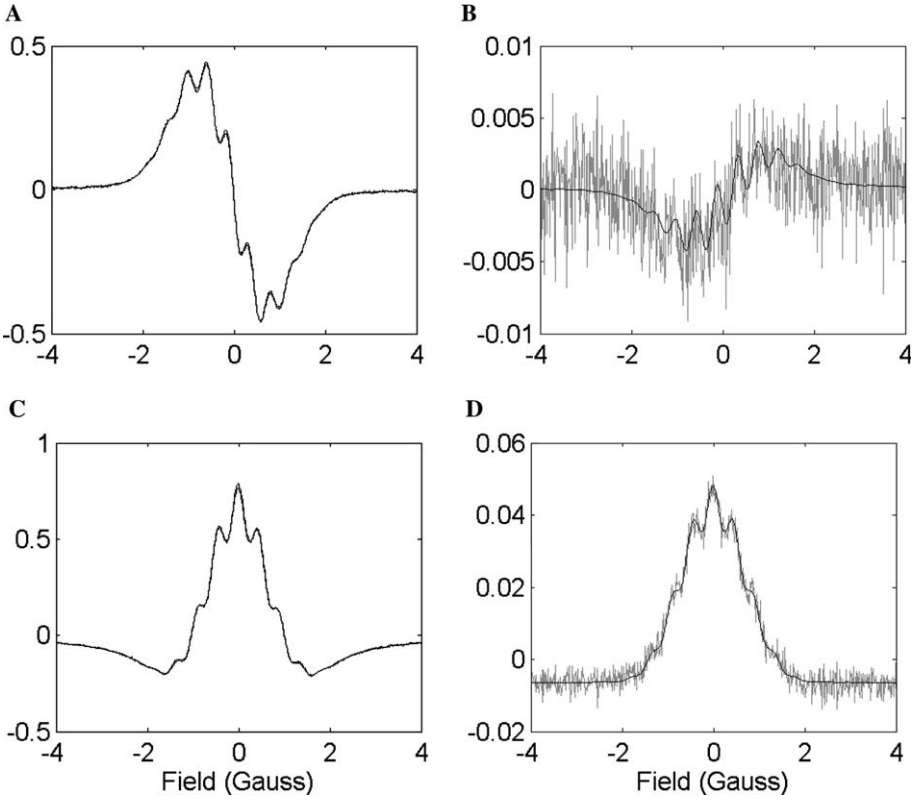

Fig. 2. First Harmonic 9.2 GHz CW EPR spectra of the center ^{14}N line of 0.25 mM $^{14}NH_{18}$ TEMPOL in H_2O at 20 °C with microwave amplitude $h_1 = 0.08$ Gauss, Zeeman $h_1 = 0.03$ Gauss peak-to-peak, and Zeeman modulation frequency of 15 kHz. All 4 ordinates are on a common but arbitrary scale. Solid lines are fits (see text) obtained by global analysis on a set of 96 CW spectra that included first and second harmonic, in phase/out of phase, and absorption/dispersion with microwave amplitudes, h_1, between 0.015 and 0.35 Gauss. Optimal relaxation rates and SHF pattern are given in Table 1 and Fig. 4. The saturation factor is $(h_1)^2/(R_1 \cdot R_2) \approx 0.5$ for the spectra shown. (A) absorption, in-phase, and first harmonic, $\chi^2 = 2.7, 1 - R^2 = 5.8 \times 10^{-4}$; (B) absorption, quadrature, and first harmonic, $\chi^2 = 1.2, 1 - R^2 = 0.77$; (C) dispersion, in-phase, and first harmonic, $\chi^2 = 4.8, 1 - R^2 = 6.6 \times 10^{-4}$; and (D) dispersion, quadrature, and first harmonic, $\chi^2 = 1.0, 1 - R^2 = 0.030$, R is the correlation coefficient relating the theoretical fit to the experiment.

0.35 Gauss using global analysis. Table 1 contains the optimal SHF coupling constants and relaxation rates. A stick pattern representation of the SHF pattern is shown in Fig. 4 (top). Only the central ^{14}N center manifold was simulated. The bottom panel of Fig. 4 shows an experimental FID for the pump situated on the center of the manifold with two simulations for comparison (see Section 2). Simulation (a) is the solution of the Bloch equations for a FID, assuming the SHF lines are independent resonance positions with the intrinsic relaxation rates found from the CW fitting (Table 1, and Section 2). The experimental FID is overlaid with the Bloch equation simulation, and exhibits a SHF echo, at $\sim$0.78 μs. For comparison, the FID resulting from a simple 7 line pattern with SHF coupling constant of 0.45 Gauss is shown as (b). The latter simplification of the SHF pattern is a minimal model using only the six equivalent protons on the equatorial methyl groups (see Table 1). In general N equivalent nuclei will give rise to a binomial SHF distribution with $N + 1$ resonance positions. The sum of the contributions to the FID from each resonance line in SHF pattern may be summed explicitly so that the FID is given by:

$$M_y \propto \cos(\delta t) \cdot \left[\cos\left(\frac{\bar{a}_{\mathrm{shf}}}{2} t\right)\right]^N \cdot \mathrm{e}^{-R_2 t}, \tag{5}$$

where δ is the offset of the pump frequency from the center of the SHF manifold, and $\bar{a}_{\mathrm{shf}}$ is the SHF splitting [43]. $N = 6$ for the six equivalent methyl protons. The FID of the 7 line pattern shown in spectrum b of Fig. 4. The experimental FID as a function of offset from the center of the SHF structure is shown in Fig. 5A. The static magnetic field was varied to produce the resonance offset. Fig. 5B is the solution of the Bloch equations as described above. Fig. 5C is the result from a simple 7-line pattern given by Eq. (5) with $N = 6$. Because Eq. (5) is equivalent to the solution to the Bloch equations, its scaling relative to the simulations given in Fig. 5B is known, and was scaled down for comparison here. The simulations in Fig. 5B for the complex SHF pattern (Fig. 4, top) exhibit greater destructive

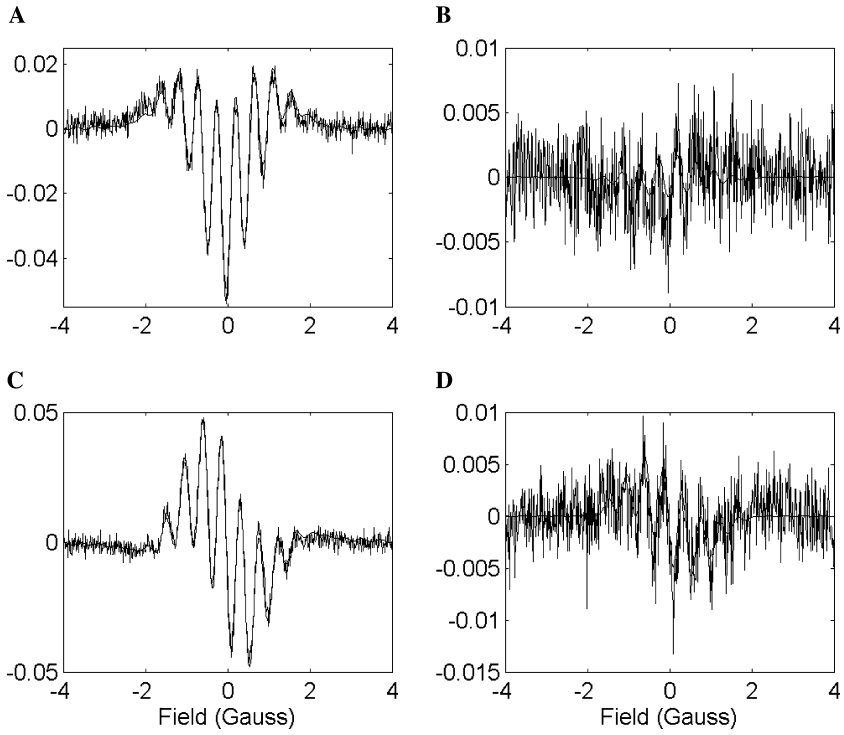

Fig. 3. Second Harmonic 9.2 GHz CW EPR spectra of the center ^{14}N line of $^{14}NH_{18}$ TEMPOL (as in Fig. 2); (A) absorption, in-phase, and second harmonic, $\chi^2 = 1.2, 1 - R^2 = 0.074$; (B) absorption, quadrature, and second harmonic, $\chi^2 = 1.0, 1 - R^2 = 0.94$; (C) dispersion, in-phase, and second harmonic, $\chi^2 = 1.0, 1 - R^2 = 0.054$; and (D) dispersion, quadrature, and second harmonic, $\chi^2 = 1.1, 1 - R^2 = 0.79$.

Table 1

Proton SHF splittings (Gauss)*						Relaxation rates	
						Gauss	Mrad/s
	2-C**H**$_{3\ eq}$	2-C**H**$_{3\ ax}$	2-C**H**$_{eq}$	2-C**H**$_{ax}$	1-C**H**	R_1 0.0930(2)	1.637(4)
$\bar{a}_H$	0.445(1)	0.0979(8)	0.417(4)	0.379(2)	0.1727(9)	R_2 0.1373(3)	2.417(6)

*Three ^{13}C (1.1% natural abundance) SHF splittings of 7.750(3), 4.999(4), and 3.496(3) Gauss were used in addition to proton SHF, and were determined from the $^{14}ND_{17}H$ TEMPOL spectrum.

interference of SHF contributions, and are 1/20 the scale of the simple 7 line SHF pattern.

The pulsed saturation recovery (pSR) spectrum was recorded both on the center of the SHF manifold, and as a function of offset. Fig. 6 shows the pSR spectrum when the observer frequency is on resonance and 0.5 Gauss off resonance. Black lines are simulations from the Bloch equations (see Section 2). The data were also fit to a single exponential after cropping the first 0.5 μs (fit not shown; the effective rate (R_{1eff}) is 1.95(1) Mrad/s). The effective spin–lattice relaxation rate R_{1eff}, obtained by cropping the first 0.5 μs of the pSR spectrum was investigated systematically as a function of pump pulse duration. Fig. 7 shows the experimental rates (open circles) as well as the results of Bloch equation simulations (black squares). In both the data and simulation the pump power was adjusted with the pump time so that the product remained consistent with a π to $4\pi/3$ pulse, and the observe microwave amplitude was 0.04 Gauss. However, a larger pump power was used for the far left point (as a long pulse), because the conjugate power for a π pulse was unattainably low. The simulations, including normally distributed noise, were then fit in the same manner as the experimental data. The conditions corresponding to the top pSR spectrum shown in Fig. 6 are the points with $1/\tau_p \cong 6$ MHz in Fig. 7. The oxygenated rate for these conditions is given in the legend of Fig. 7. The maximum of the R_{1eff} rates, shown in Fig. 7, occurs at an inverse pump time of ~1.2 MHz.

We studied the deuterated TEMPOL nitroxide by TD methods. Fig. 8 shows the FID obtained from the center manifold of ^{14}N $D_{17}H$ TEMPOL with and without oxygen (air). The overlaying fit contains the product of an exponential and a Gaussian decay. The Gaussian decay approximates the deuteron SHF structure, and arises from the Fourier transform analog of the Voightian lineshape, which is the convolution of a Gaussian and

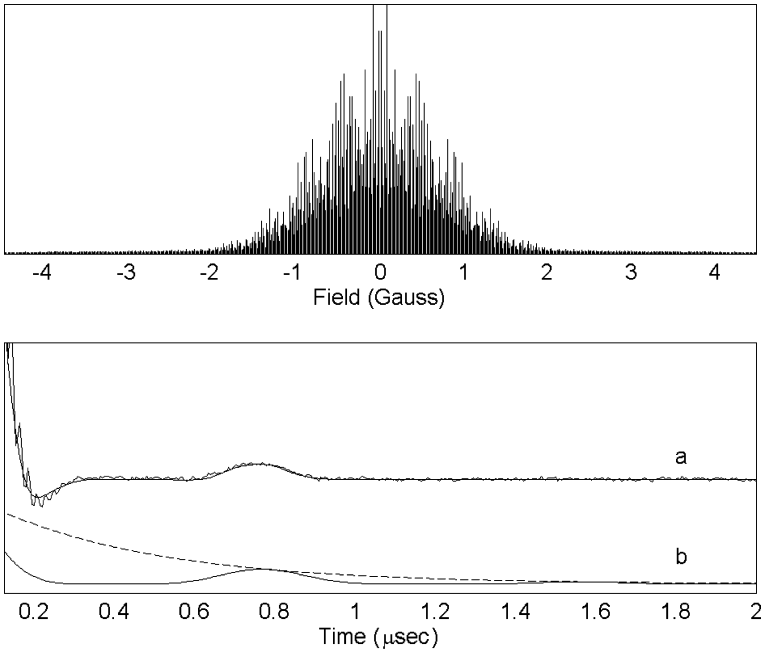

Fig. 4. FID resulting from the SHF proton and carbon structure of $^{14}NH_{18}$ TEMPOL. (top) Optimal SHF pattern found in fitting of CW spectra (see Table 1). (bottom) Experimental FID and simulation of the FID from the Bloch equations under the assumption that the SHF structure results in independent resonance conditions. The rates obtained from CW fitting (Table 1) and experimental pulse conditions ($\approx 9\pi/4$ pulse) were used in the simulations. The simulations were done with no adjustable parameters. (a) Experimental FID with Bloch equation simulation overlaid (see Fig. 5 below). (b) FID for a simple seven line pattern (see text, Eq. (5)) with splittings of 0.45 Gauss. Superimposed is a single exponential decay using rate R_2 from Table 1 (dashed line).

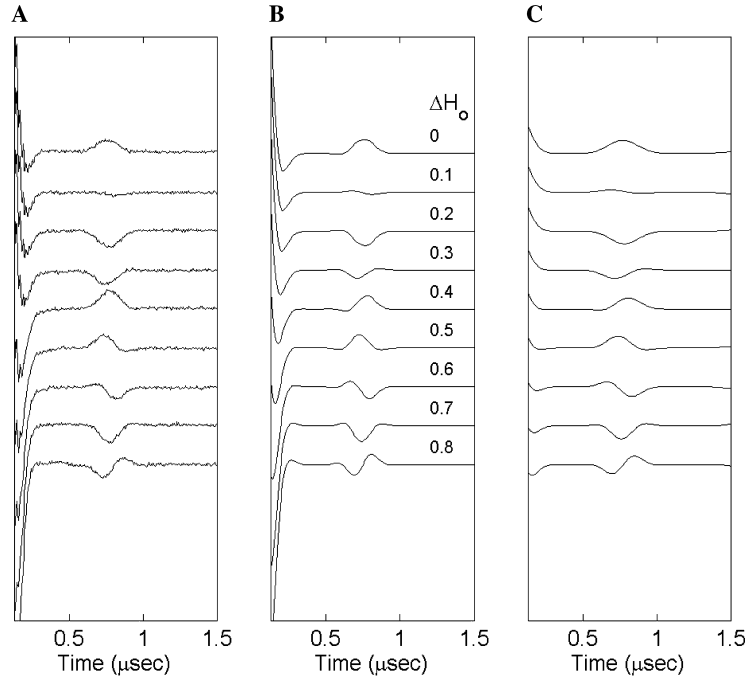

Fig. 5. FID of $^{14}NH_{18}$ TEMPOL (Fig. 4). (A) Experimental FID, as a function of resonance offset from the center ^{14}N line (0–0.8 Gauss offset, offset top to bottom in increments of 0.1 Gauss of the Zeeman field). Pump time was 130 ns, h_1 was ~3 Gauss, and 90 ns dead time (using a $9\pi/4$ pulse). (B) Simulation using the Bloch equations with the hyperfine pattern and relaxation rates obtained from CW fitting (Figs. 2–4 (top), and Table 1), and experimental pump/field conditions. All simulations are on a common scale, with no adjustment of relative scaling, but have been offset on the ordinate as a function of field offset for comparison with (A). (C) Analytic formula for a simple seven line binomial SHF distribution with splitting of 0.45 Gauss (see text, Eq. (5)).

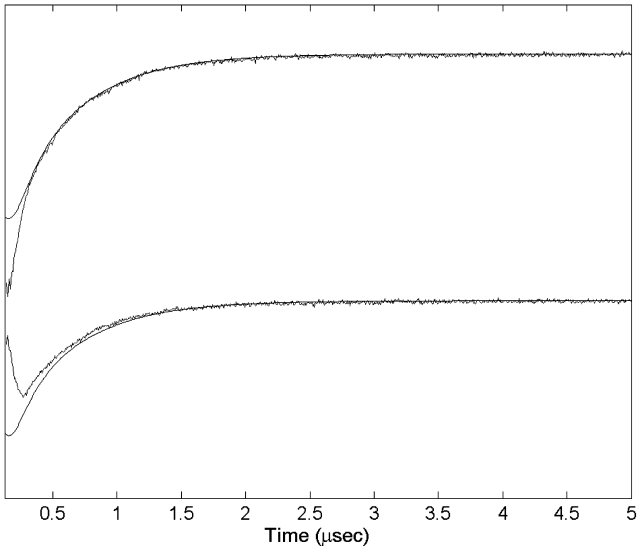

Fig. 6. Experimental pulsed saturation recovery on the ^{14}N center manifold of $^{14}NH_{18}$ TEMPOL, with 170 ns pump time, ~1.5 Gauss pump amplitude ($4\pi/3$ pulse), and 0.04 Gauss observing microwave amplitude. Solid lines are simulations using the Bloch equations for all of the SHF lines shown in Fig. 4, assuming independent SHF resonances, and using the rates obtained from fitting of linear and saturated CW spectra (Table 1) with experimental pump/field conditions. The top spectrum is for the resonance frequency set to the center of the SHF manifold, the bottom is 0.5 Gauss offset. The two simulations are on a common scale, with no relative adjustment. The common simulation scale was adjusted to have optimal agreement with the top spectrum. Aside from a scaling to fit the data, the simulations used no adjustable parameters. Fitting the experimental pSR spectrum for the on resonance condition (top spectrum) to a single exponential, neglecting the beginning 0.5 μs, gives an effective R_1 rate of 1.95(1) Mrad/s. The same effective rate, within fitting error, is obtained from the bottom spectrum.

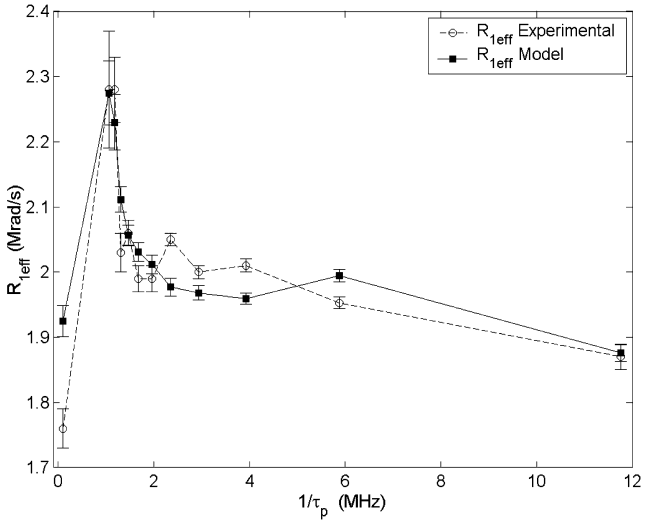

Fig. 7. Effective spin–lattice relaxation rates ($R_{1,\mathrm{eff}}$) obtained from experimental and theoretical pSR spectra of deoxygenated $^{14}NH_{18}$ TEMPOL (as in Fig. 6). The theory (see text) consists of Bloch equation simulations with the CW-determined SHF splittings, R_1 (1.6 Mrad/s) and R_2 (2.4 Mrad/s) rate (see Table 1), and experimental pump time/power conditions. Effective rates were obtained from a single exponential fit to the experimental or theoretical pSR spectrum, neglecting the first 0.5 μs. Pump time/power conditions were consistent with a π pulse for all data points except the longest pump time (far left datum) where a 5π pulse was applied. Connecting lines are for visualization. The experimental effective rate in the presence of O_2 (air) at 170 ns pump time ($1/\tau_p \cong 6$ MHz) is 3.62(2) Mrad/s (not shown on figure). 3.76(2) Mrad/s was obtained from the simulations for this condition when 2 Mrad/s was added to the fundamental R_1 and R_2 rates in accordance with oxygen relaxation observed independently on deuterated TEMPOL (see Fig. 8 legend).

Lorentzian lineshape in the CW domain [14,44]. The functional form of the FID is:

$$M_y \propto e^{-R_2 t} \cdot e^{-\frac{\sigma^2}{2}t^2}. \quad (6)$$

Because Gaussian spectral width, σ, represents SHF structure is does not change with oxygen concentration. The R_2 rate—extracted with Eq. (6) in the absence of O_2—changed by 2.13(4) Mrad/s upon addition of O_2 (see Fig. 8, legend). For comparison, Fig. 8 shows the best fit of the FID to a single exponential, with no Gaussian component. The fit of a single exponential is noticeably worse and the R_2 rate is quite different.

3.2. Comparison of CW and TD measured relaxation parameters for hGIIA $sPLA_2$: motional dependence and spin-relaxant measurements

We have studied the binding of the 14 kDa protein hGIIA $sPLA_2$ to two lipid systems using spin relaxant techniques [34]. We present data to illustrate the relative sensitivities of CW and TD relaxation measurements for a system under conditions typical to biological experiments: i.e., using 2–5 μL of a 45 μM protein solution, and a single spin-label per protein attached through a flexible linkage to a cysteine sulfhydryl group. We also present both TD and CW measurements on [^{14}N]dCTPO in viscous glycerol solutions as a reference for interpreting the motional dependence of the spectra. Relaxation of the spin-label bound to hGIIA $sPLA_2$ by molecular oxygen, when the enzyme is either free in solution or bound to large unilamellar vesicles (LUV) is used to compare collision-induced relaxation rates obtained from the CW power saturation technique with R_1 relaxation obtained from pSR measurements. Relaxation of spin-labeled hGIIA $sPLA_2$ by the charged spin relaxant CROX further illustrates how TD and CW methods compare.

Fig. 9 shows the model nitroxide [^{14}N]dCTPO in 85% v/v glycerol/water solvent at several temperatures (left panel), and ^{14}N spin-labeled 14 kDa protein hGIIA $sPLA_2$ that is bound to mixed micelles (average diameter 100 Å) for several different labeling sites of the protein (right panel). The nitroxide in glycerol represents isotropic motion and is arranged according to temperature, which has been converted into an isotropic rotational correlation time using a model of glycerol–water

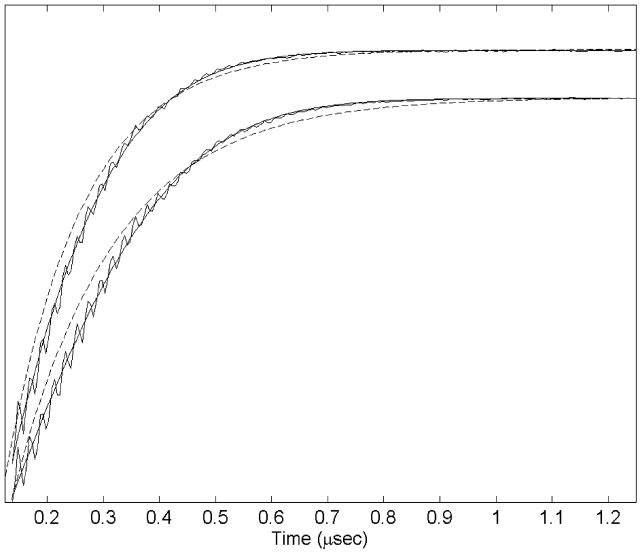

Fig. 8. FID for the center ^{14}N line of 0.25 mM $^{14}ND_{17}$ TEMPOL in H_2O at 20 °C with 130 ns pump time, and ~3 Gauss pump amplitude. The top spectrum is with O_2 (air); and the bottom spectrum is without O_2. The first 1.25 μs of a 5 μs acquisition is shown. Solid lines are fits to the product of a Gaussian and an exponential decay. The Gaussian σ (Eq. (6)) is 3.44(4) Mrad/s. The exponential component with O_2 is 4.36(4) Mrad/s and without O_2 is 2.23(2) Mrad/s. The dashed lines are the best fit to a single exponential (7.29(5) Mrad/s, with O_2 and 5.55(3) Mrad/s, without O_2). The 48 MHz oscillation in the data is the ^{14}N hyperfine due to the other resonance positions −17.13(5) and +17.22(5) Gauss away (as measured from the CW spectrum).

viscosity [23,37]. The spectra of hGIIA $sPLA_2$ on mixed-micelles are arranged by accessibility of the nitroxide to the solution phase, as determined by exposure to spin relaxants CROX and NiEDDA using pulsed pSR [21,34]. In our study S35, S120, and T104 were found to be exposed to solution, whereas V3, L19, and F23 surrounded the binding surface of the protein on DTPM mixed micelles [34]. The protein data exhibits a correlation of spin-label mobility with accessibility to the aqueous environment. The peak-to-peak linewidth shown on the figure is measured from the center of the spectrum and is expressed in Gauss.

Fig. 10 (top) shows R_1 from pSR and pELDOR for [^{14}N]dCTPO in 85 and 100% v/v glycerol/water solvent over a range of temperatures that have been converted to rotational correlation time [23,37]. A spin-nuclear relaxation rate (R_{1n}) was included in fitting of the pSR spectrum, but always exceeded the R_1 value by greater than an order of magnitude, and so could have been excluded in fitting. The spin lattice relaxation rate of the [^{14}N]dCTPO radical is observed to change by a factor of 6 for a factor of 400 change in correlation time over the range shown. The spin lattice relaxation rate of hGIIA $sPLA_2$ bound to mixed micelles (bottom) is seen to range over values that differ by a factor of 2 depending upon labeling position. The variation of R_1 is correlated with the variation in mobility implied by the CW spectra (Fig. 9), as well as the accessibility to solvent phase as

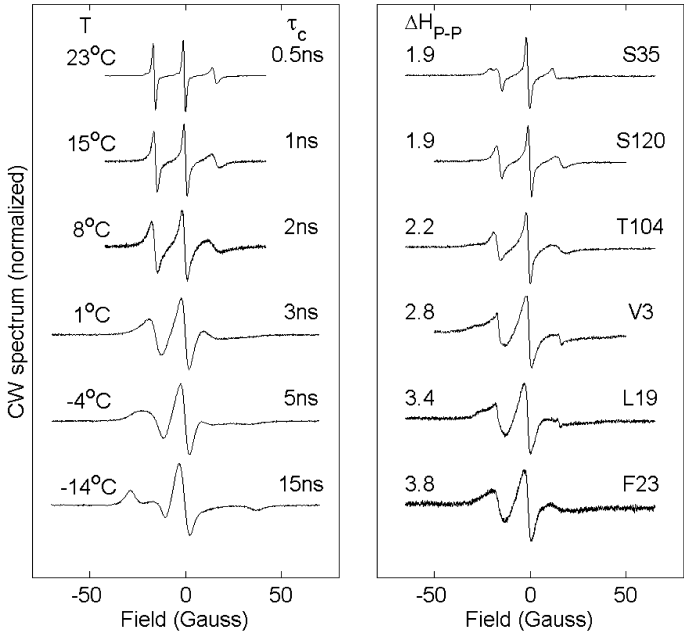

Fig. 9. (left) 9.2 GHz linear EPR spectra of 0.5 mM $^{14}ND_{13}$ CTPO in 85% v/v glycerol/water solutions at several temperatures. Correlation times are calculated assuming CTPO is a sphere of hydrodynamic radius 3.1 Å and from values of glycerol/water viscosity [37]. Spectra are scaled to unit peak-to-peak height. (right) Linear EPR spectra ~45 μM ^{14}N MTSSL spin-labeled hGIIA $sPLA_2$ bound to mixed micelles of 12.6 mM DTPM/126 mM Triton X-100 (30 acquisitions, ~40 min acquisition time) spin-labeled at various sites. Numbers are labeling position, and letters are the native residue before mutation to cysteine for spin labeling. Spectra are arranged top to bottom according to decreasing solvent accessibility of the spin label [34]. The peak-to-peak linewidth measured from the center of the spectrum, ΔH_{p-p}, is given in Gauss on the figure.

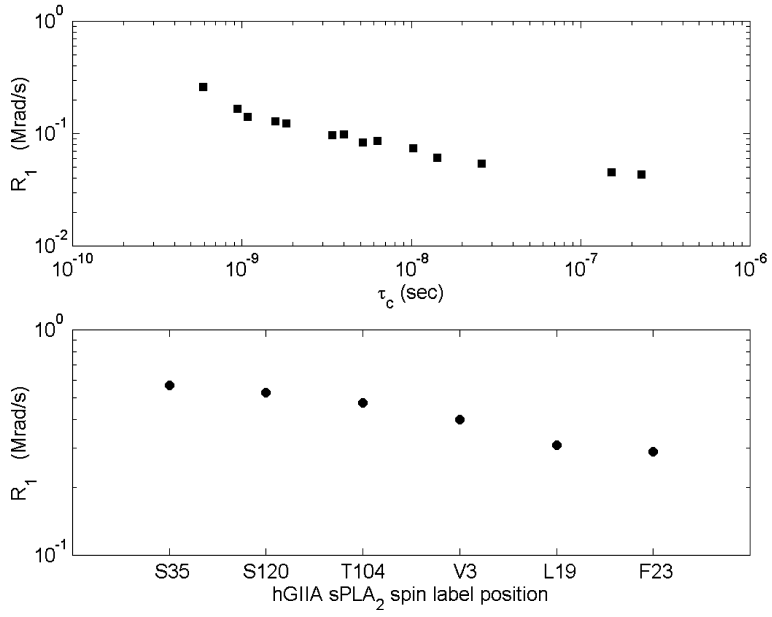

Fig. 10. Experimental spin–lattice relaxation rates ($R_1 \equiv \frac{1}{T_1}$) from pSR and pELDOR with the observing frequency on the center of the ^{14}N manifold. For pELDOR the pump frequency was placed on the low field manifold. (top) 0.1 mM $^{14}ND_{13}$ CTPO in 85 and 100% v/v glycerol/water solutions for various temperatures plotted as a function of the correlation time (calculated according to a model of glycerol/water viscosity [37]). An R_{1n} rate was included in fitting of pSR and pELDOR spectra, but exceeded 10 Mrad/s (not shown in figure). Errors are within the size of the symbols. (bottom) R_1 rates for 2 μL of ~ 45 μM spin-labeled hGIIA sPLA$_2$ on mixed micelles of 10% DTPM/Triton X-100 (5 M acquisitions, ~20 min acquisition time), see Table 2 column 8 for all sites. Spin labeling positions are arranged on the *x*-axis left-to-right according to decreasing solvent accessibility of the spin-label to the spin relaxants CROX and NiEDDA [34].

determined by CROX/NiEDDA relaxation studies [21,34]. A more complete set of data for hGIIA sPLA$_2$ in solution and on mixed micelles is provided in Table 2. Table 2, columns 4 and 8 illustrate the change in R_1 which results from binding to mixed micelles. Column 9 of Table 2, the R_1 rate of hGIIA bound to mixed

Table 2
pSR and CW power saturation data for the enzyme hGIIA sPLA$_2$ in solution and bound to mixed micelles of 10%DTPM/Triton X-100

	Solution[a]				Solution[a]			Mixed micelles[b]	
	N_2[c]				O_2[d]			N_2[c]	O_2[d]
	P_2[e] (Gauss^2)	ε[e]	R_2[f] (Gauss)	R_1[g] (Mrad/s)	P_2 (Gauss^2)	ε	R_1 (Mrad/s)	R_1 (Mrad/s)	R_1 (Mrad/s)
V3	0.051(3)*	1.02(3)	1.8	0.519(6)	0.22(1)	1.08(3)	1.51(2)	0.401(3)	1.20(1)
K10	0.068(5)	1.16(4)	2.0	0.356(5)	0.24(2)	0.98(3)	1.35(2)	0.282(5)	0.82(2)
L19	0.063(2)	1.07(1)	1.5	0.560(4)	0.20(1)	1.00(2)	1.83(3)	0.309(5)	1.01(2)
F23	0.041(3)	1.13(3)	1.7	0.393(5)	0.15(1)	1.11(4)	1.39(3)	0.288(8)	0.84(3)
S35	0.046(3)	1.22(3)	1.6	0.48(1)	0.107(4)	1.03(2)	1.7(2)	0.566(5)	1.35(2)
K56	0.065(3)	1.11(2)	1.7	0.508(5)	0.196(9)	0.99(2)	1.66(3)	0.392(9)	0.57(2)
F63	0.063(4)	1.16(3)	1.5	0.516(7)	0.19(1)	1.06(3)	1.57(3)	0.297(4)	1.14(3)
N70	0.064(2)	1.12(1)	1.9	0.370(4)	0.20(1)	0.99(2)	1.34(4)	0.454(4)	1.07(2)
T104	—	—	1.7	0.442(5)	—	—	1.35(3)	0.464(3)	1.06(1)
S113	0.059(4)	1.03(3)	1.6	0.579(6)	0.17(1)	0.95(3)	1.72(4)	0.538(7)	1.05(1)
K115	0.057(3)	1.07(3)	1.6	0.568(6)	0.22(2)	1.09(3)	1.75(4)	0.273(7)	0.97(3)
S120	0.060(2)	1.11(2)	1.4	0.619(4)	0.184(9)	1.05(2)	1.88(3)	0.527(5)	1.28(2)

Spin–lattice relaxation rates ($R_1 = 1/T_1$) are in Mrad/s.
[a] 40–50 μM hGIIA, 50 mM Tris–HCl, pH 8.0, 0.5 mM $CaCl_2$, 21 °C.
[b] 12.6 mM DTPM, 126 mM Triton X-100.
[c] Samples degassed in the LGR resonator, by exchange through Teflon sample tube.
[d] Compressed air (21% O_2).
[e] Obtained from least squares fit of CW power saturation data using Eq. (1).
[f] Estimated with an experimental uncertainty of 0.1 Gauss from the CW first harmonic absorption peak-to-peak linewidth.
[g] π pulse and 0.04 Gauss observing microwave amplitude.
[*] All values reported as 0.051 ± 0.003, where the error is from the fitting.

micelles in the presence of O_2 (air), is given to show how oxygen exposure may be modified by the presence of the mixed-micelle binding substrate, and supplements the data obtained with LUVs shown in Figs. 12 and 13 below.

Figs. 11–13 compare TD and CW measured oxygen collisional relaxation of ^{14}N spin-labeled hGIIA $sPLA_2$ in the presence and absence of binding to vesicles of negatively charged lipid (see Section 2), for a set of spin labeling sites on the surface of the protein. In this system the vesicles aggregate in such a way that the $sPLA_2$ protein is occluded from the aqueous phase [34]. Aggregation of vesicles is promoted by the high positive electrostatic charge on the hGIIA enzyme, which has a pI of 9.39 (see electrostatic measurements with EPR discussed below in this section) [34]. This is to be distinguished from the binding of hGIIA to the mixed micelles presented above (Figs. 9 and 10). No aggregation occurs for that system and some spin-labeled sites are exposed to solvent when bound to the mixed micelles while others are in contact with the micellular surface.

Fig. 11 shows the O_2 (air) induced fractional change of R_1 determined by pSR, and the analogous quantity of P_2 from CW progressive saturation for the hGIIA enzyme in the absence of any membrane binding. The CW measurement $\Delta P_2/P_2^0$ is plotted vs. the TD measurement $\Delta R_1/R_1^0$. The spin labeling sites on the hGIIA enzyme are given adjacent to the data points in the figure. This figure is presented as a diagnostic for direct comparison of the CW and TD relaxation measurements. Eqs. (2) and (3) predict that the fractional change of R_1 and P_2 should give the same values. The solid lines in Fig. 11 represent complete correlation of the TD and CW values. The left vs. right panels represent two different ways of analyzing the CW power saturation data. The time domain values are the same in both panels. The left figure is the result of allowing a separate ε parameter (see Eq. (1)) for fitting oxygenated and deoxygenated saturation "rollover" data. Columns 1–7 of Table 2 contain the ε, P_2, and R_1 values for the hGIIA labeling sites shown in Fig. 11, left. The right figure is the result of insisting that a common ε value is used while fitting the oxygenated and deoxygenated data to obtain $P_2^{+O_2}$ and $P_2^{-O_2}$. When ε is constrained to be the same when fitting $P_2^{+O_2}$ and $P_2^{-O_2}$ data, then the values of ε decrease by 1–10% for the no oxygen condition, and increase by 1–10% for the oxygenated condition (Table 2 and column 2 and Table 4 column 3). These changes deviate by less than an order of magnitude from the fitting error inherent in ε (see Table 2 columns 2 and 6). The ε constraint decreases $P_2^{-O_2}$ by 4–16% (Table 2 and column 1 and Table 4 column 1) and increases $P_2^{+O_2}$ by 4–13%

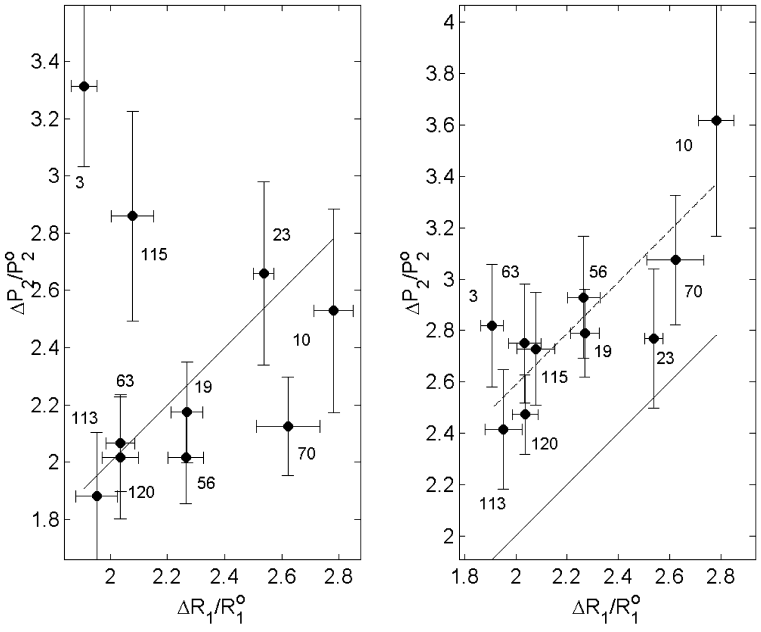

Fig. 11. Comparison of the O_2 (air) induced fractional change of relaxation parameters R_1 from pulsed (TD) and P_2 from CW EPR, for ~45 μM spin-labeled hGIIA $sPLA_2$ in aqueous solution at 20 °C. R_1 was measured on the center manifold of the ^{14}N nitroxide spin-label by pSR. P_2 was measured from the center manifold peak-to-peak height ΔY by progressive saturation of the CW spectrum. According to Eq. (2) both quantities (on the abscissa and the ordinate) should be the same quantity, which is $\chi \cdot [O_2]/R_1^0$. Therefore, the solid lines represent complete correlation between the CW and TD methods. The numbers adjacent to data points represent the labeled residue on the hGIIA $sPLA_2$ enzyme. Error bars are calculated from the fitting errors in Table 2. (left) P_2 determined by floating the ε parameter independently for $\pm O_2$ conditions (Eq. (1) and Table 2 columns 1 and 5). (right) P_2 determined by constraining ε parameter to be the same for $\pm O_2$ conditions(Table 4 columns 1 and 2). The best fit line with unit slope is given by the dashed line.

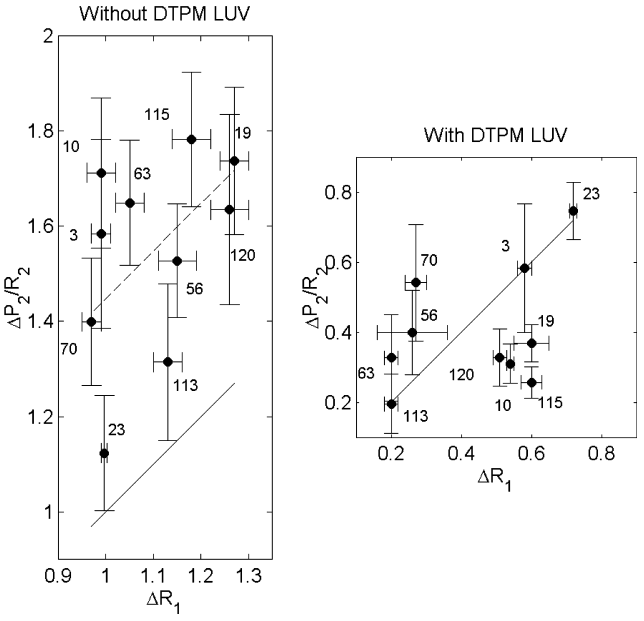

Fig. 12. Comparison of the oxygen collisional relaxation $\chi[O_2]$, measured by SR and CW power saturation for spin-labeled hGIIA $sPLA_2$ in solution (left) and bound to large unilamellar vesicles (LUV) of 25 mM DTPM lipid (right). Solid lines represent complete correlation between the CW and TD methods. All rates are in Mrad/sec. (left) ΔR_1 measured on the center of the ^{14}N manifold from R_1 with and without O_2 for hGIIA in solution (see Table 2). ΔP_2 from P_2 values with and without oxygen. P_2 values used consisted of the average value from fitting strategies where ε parameters were either independent or constrained to be the same value for $\pm O_2$ conditions (Tables 2, 4, and text). (right) ΔR_1 measured on the center of the ^{14}N manifold from R_1 with and without O_2 for hGIIA bound to vesicles. ΔP_2 from P_2 values with and without oxygen for hGIIA bound to vesicles. P_2 values used consisted of the average value from fitting strategies where ε parameters were independent or constrained to be the same value for $\pm O_2$ conditions (Tables 3, 4, and text).

(Table 2 and column 5 and Table 4 column 2). These changes are again within an order of magnitude of the fitting error on P_2. The changes seen between the left and right panels of Fig. 11 result from the combined effect of the ε constraint on both $P_2^{+O_2}$ and $P_2^{-O_2}$.

Fig. 12 compares $[O_2]$ induced ΔR_1 from TD measurements with $\Delta P_2/R_2^0$ from CW measurements for hGIIA $sPLA_2$ in the absence of vesicles (left) and bound to vesicles (right). Eqs. (3) show that these two quantities should both be equal to $\chi \cdot [O_2]$. The R_2^0 value used was estimated from the central CW linewidth, following the standard method for estimating R_2^0 in progressive saturation [2,11,45]. The CW progressive saturation data was analyzed by the two methods presented in the description of Fig. 11 above. The values of $\Delta P_2/R_2^0$ given in Fig. 12 consist of the arithmetic average of the optima found from the two fitting strategies (e.g., Table 3 columns 1,5 and Table 4 columns 4,5). It should be noted that the ε and P_2 parameters are more sensitive to the choice of fitting protocol in the case of membrane binding (Tables 3 vs. 4). The solid lines in both panels represent complete correlation between the TD and CW measurements. When the enzyme is not bound to vesicles (left), the value of $\chi[O_2]$ given by the CW technique is larger than the value measured by TD by 40% on average, and is indicated by the dashed line.

Fig. 13 compares the values of the oxygen exposure factor, Φ (see, Eq. (4)), calculated from the change in R_1 (Φ_{TD}) and two CW estimates, using changes in P_2 (Φ_{CW}). Φ reflects the oxygen relaxation at each spin labeling site for hGIIA bound to vesicles relative to the unbound state where the enzyme is free in solution. Φ_{CW}, computed by the two different methods, is plotted against Φ_{TD} as a scatter plot to display how consistent the TD and CW values are. Solid lines represent complete correlation between TD and CW values. The exposure factors determined from the CW measurements are presented both as the direct ratio of ΔP_2's for the vesicle and solution conditions (left), and alternatively with ΔP_2 values scaled individually by the CW peak-to-peak linewidths (R_2^0) for the vesicle and solution conditions (right). The peak-to-peak linewidths increase by between a factor of 1.3 and 2.7 amongst the various labeling sites as a result of membrane binding (see Table 2 column 3 and Table 3 column 3). Therefore, the individual scaling of ΔP_2's by the linewidth for solution and membrane conditions represents a potentially significant correction to Φ.

Collisional relaxation of sl-hGIIA $sPLA_2$ by the relaxing agent CROX provides another example of the application of both TD and CW techniques in the biological regime. The high positive protein surface charge of $sPLA_2$ previously mentioned, was quantified by measuring the collisional relaxation due to CROX (nominal charge 3-) at spin-labeled sites on protein free in solution. Fig. 14 illustrates the effect of CROX on the spin-label at site S35C-sl. The left panel shows the centerline manifold of the ^{14}N nitroxide as a function of CROX concentration. For a concentration of 10 mM CROX ~4.5 Gauss of linewidth broadening was observed for S35C-sl instead of the ~0.5 Gauss expected for a spin-labeled neutral protein under the same electrolyte conditions [46,47]. This enhancement of Crox relaxivity implies a local positive protein surface potential (Ψ) on the order of +25 mV. Assuming a simple electrostatic Boltzmann distribution, and using the $z = -3$ as the nominal charge of Crox, the surface potential is given by the ratio $\frac{[Crox]}{[Crox]_0} \approx \frac{4.5}{0.5} = e^{-z\Psi/k_B T}$ [48]. The right panel shows how relaxation of 0.5 mM CROX may be modulated by the presence of NaCl as a salting effect. The effect of 0.5 mM CROX on the lineshape of a spin-labeled neutral protein with similar electrolyte composition (50 mM buffer) is expected to be negligible [10]. Addition of 175 mM NaCl is sufficient to screen the strong electrostatic effect found in the case of hGIIA $sPLA_2$ and restore the lineshape (Fig. 14, right panel, top). Either a TD measurement of R_1 relaxation

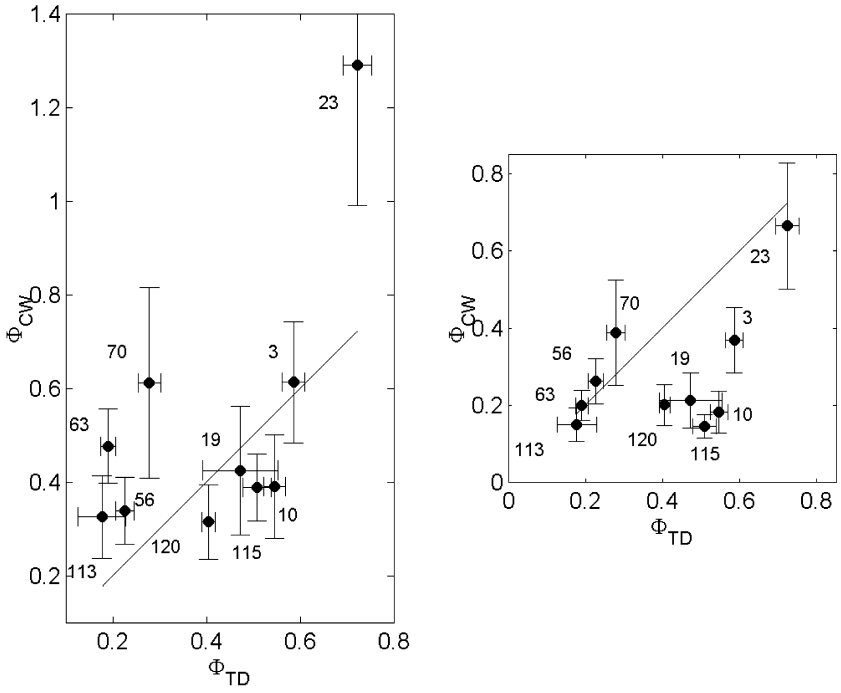

Fig. 13. Φ, the ratio of oxygen relaxation when bound to vesicles (DTPM LUV) vs. free enzyme in solution using the changes in relaxation shown in Fig. 12 (see Eqs. (3) and (4)). Solid lines represent complete correlation between the CW and TD methods. For both left and right panels: $\Phi_{TD} = (\Delta R_1^{vesicles}/\Delta R_1^{solution})$, (left) $\Phi_{CW} = (\Delta P_2^{vesicles}/\Delta P_2^{solution})$, (right) $\Phi_{CW} = (\Delta P_2^{vesicles}/R_2^{0,vesicles})/(\Delta P_2^{solution}/R_2^{0,solution})$, R_2 measured from the linear CW linewidth (see text, and Table 2).

Table 3
pSR and CW power saturation data for the enzyme hGIIA sPLA$_2$ bound to large unilamellar vesicles of DTPM

	Membrane (DTPM LUV)						
	N_2				O_2		
	P_2 (Gauss^2)	ε	R_2 (Gauss)	R_1 (Mrad/s)	P_2 (Gauss^2)	ε	R_1 (Mrad/s)
V3	0.050(4)	0.91(3)	3.0	0.45(1)	0.111(6)	0.67(1)	1.03(2)
K10	0.058(6)	1.13(5)	4.3	0.259(5)	0.102(8)	0.78(2)	0.78(2)
L19	0.052(5)	1.03(5)	3.0	0.372(6)	0.07(1)	0.60(3)	1.31(2)
F23	0.049(4)	1.02(3)	3.3	0.262(7)	0.14(2)	0.75(5)	0.98(3)
S35	0.022(1)	0.94(1)	2.2	—	0.065(5)	1.03(3)	—
K56	0.044(3)	0.90(3)	2.2	0.603(8)	0.10(1)	0.96(5)	0.95(1)
F63	0.056(3)	1.08(2)	3.6	0.297(3)	0.088(9)	0.76(3)	0.773(8)
N70	0.051(4)	0.97(3)	3.0	0.307(6)	0.13(2)	0.87(5)	0.61(2)
T104	—	—	—	—	—	—	—
S113	0.029(4)	0.67(2)	3.5	0.85(2)	0.055(5)	0.57(1)	1.64(3)
K115	0.051(7)	0.86(5)	4.3	0.30(1)	0.101(7)	0.77(2)	0.90(3)
S120	0.059(3)	0.97(2)	2.2	0.422(7)	0.079(8)	0.76(3)	1.04(1)

Spin–lattice relaxation rates ($R_1 = 1/T_1$) are in Mrad/s.
(See legend to Table 2).

or the CW method of power saturation may be used to quantitatively measure the salt dependence of CROX relaxation. Assuming that the protein presents a locally uniform surface potential ϕ_0, and that the effect of NaCl electrostatic screening may be treated independently as a 1-to-1 electrolyte effect, the screened protein potential, $\phi(r,[\mathrm{NaCl}])_{\mathrm{screened}}$, at a distance r from the protein surface is given by [48]:

$$\tanh\left(\frac{\phi(r,[\mathrm{NaCl}])_{\mathrm{screened}}}{4k_{\mathrm{B}}T}\right) = \exp\left\{-r\sqrt{\frac{8\pi[\mathrm{NaCl}]}{\varepsilon k_{\mathrm{B}}T}}\right\}\tanh\left(\frac{\phi_0}{4k_{\mathrm{B}}T}\right). \quad (7)$$

For a surface potential on the order of kT Eq. (7) may be linearized in $\phi(r,[\mathrm{NaCl}])_{\mathrm{screened}}$ and $\phi_0 = \phi(0,0)$. The

Table 4
CW solution and membrane data from Tables 2 and 3, re-analyzed with a common ε parameter for both N_2 and O_2 conditions by global analysis

	Solution			Membrane		
	N_2 P_2 (Gauss^2)	O_2 P_2 (Gauss^2)	ε	N_2 P_2 (Gauss^2)	O_2 P_2 (Gauss^2)	ε
V3	0.055(3)	0.21(1)	1.05(2)	0.032(4)	0.17(2)	0.78(3)
K10	0.053(4)	0.27(2)	1.04(3)	0.032(4)	0.14(2)	0.89(4)
L19	0.057(2)	0.216(8)	1.02(2)	0.022(5)	0.13(2)	0.75(5)
F23	0.039(2)	0.147(8)	1.11(3)	0.041(4)	0.23(2)	0.95(3)
S35	0.037(2)	0.124(6)	1.10(3)	0.024(1)	0.056(3)	0.97(2)
K56	0.056(3)	0.220(9)	1.04(2)	0.048(4)	0.092(8)	0.94(3)
F63	0.056(3)	0.21(1)	1.10(2)	0.038(5)	0.14(1)	0.93(4)
N70	0.054(3)	0.22(1)	1.04(2)	0.044(5)	0.15(2)	0.91(3)
T104	—	—	—	—	—	—
S113	0.053(3)	0.181(9)	0.98(2)	0.022(3)	0.074(7)	0.63(2)
K115	0.059(3)	0.22(1)	1.08(2)	0.044(5)	0.12(1)	0.82(3)
S120	0.055(2)	0.191(7)	1.07(2)	0.040(4)	0.102(9)	0.83(3)

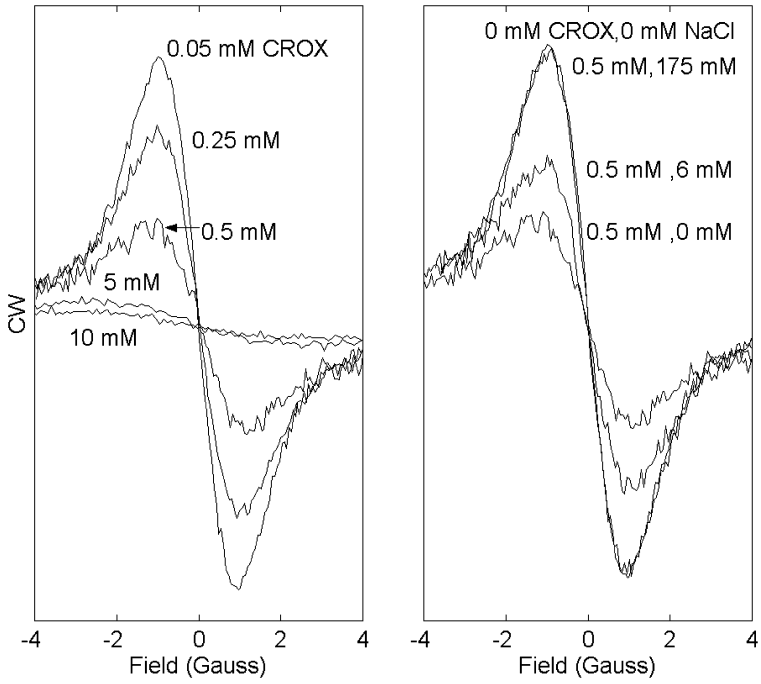

Fig. 14. CW center manifold of ^{14}N MTSSL spin-labeled hGIIA sPLA$_2$ site S35C-sl (left) as a function of [CROX] and (right) as a function of [NaCl] for fixed CROX concentration. Other electrolytes included 50 mM Tris/HCl, pH 8.0, and 0.5 mM $CaCl_2$ in all cases.

expression for $\phi(r,[\mathrm{NaCl}])_{\mathrm{screened}}$ may then be used to give the concentration of CROX as a function of distance from the surface. At the surface,

$$\chi\cdot[\mathrm{CROX}] = \chi_0\cdot[\mathrm{CROX}]\cdot\exp\left\{-\left(\frac{z_{\mathrm{crox}}\phi_0}{k_{\mathrm{B}}T}\exp\left\{-r_0\sqrt{\frac{8\pi}{\varepsilon k_{\mathrm{B}}T}[\mathrm{NaCl}]}\right\}\right)\right\}, \quad (8)$$

where r_0 is approximately the diameter of CROX ($\sim$5 Å). Fig. 15 shows $\chi\cdot[\mathrm{CROX}]$ (Eqs. (3)) measured by pSR from ΔR_1 (squares) and by CW from $\Delta P_2/R_2^0$ (diamonds). The solid line is Eq. (8) for a $\phi_0 = +25$ mV protein surface potential. Response to the neutral relaxing agent NiEDDA was measured under similar salt conditions by CW techniques and showed no dependence on NaCl concentration, as expected.

The surface potential at another site (S120) was tested by an alternative TD method. This method uses both charged and neutral relaxants and corroborates the results found using CROX. The surface electrostatic potential at site S120C-sl was measured by pSR on the center ^{14}N line of the spin-labeled protein from the ΔR_1 response to positive (TEMPAMINE), negative

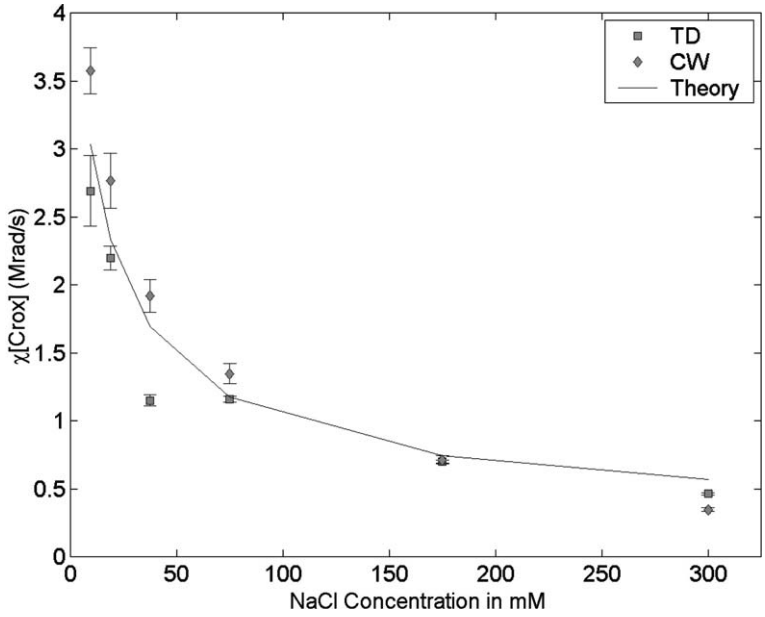

Fig. 15. ^{14}N MTSSL spin-labeled hGIIA sPLA$_2$ site N70C-sl: SR and CW power saturation measured 0.5 mM CROX relaxivity as a function of NaCl concentration. ΔR_1 (squares), $\Delta P_2/R_2^0$ (diamonds), and Eq. (8) (solid line). ε was constrained to be the same for all salt concentrations when determining P_2 by the progressive saturation method. The R_2^0 necessary for comparison of SR and CW was 25% larger than the measured peak-to-peak linewidth (see Section 4 in text). Electrolytes besides CROX and NaCl included 50 mM Tris/HCl, pH 8.0, and 0.5 mM $CaCl_2$.

(Carboxy-CTPO), and neutral (TEMPOL) ^{15}N nitroxides present in solution at 1 mM concentration (see Section 2) [10,17,49,50]. Use of ^{15}N nitroxides as a relaxing agents allows for resolution of the protein's ^{14}N center line. All three ^{15}N nitroxides are similar in size and relaxivity, so that the ratio of relaxation induced by the charged nitroxides with respect to the neutral nitroxide reflects the electrostatic Boltzmann factor [50]. These measurements yielded a protein-surface potential of $+(21 \pm 3)$ mV (data not shown); which is reasonably close to that determined from the salt effect.

3.3. CW and TD measured relaxation parameters for spin-labeled duplex DNA: motional dependence and spin-relaxant measurements

CW EPR, using a spin-label that is integral to the duplex DNA, has been used to study the flexibility of DNA [5,35,51]. The spin label's motion is slowed in comparison to the example presented by the hGIIA sPLA$_2$ enzyme above because the probe is rigidly incorporated into the DNA [52]. TD and CW measurements are shown here to illustrate how the methods for extraction of rate information are applied in this regime of slower dynamics. Fig. 16 shows the linear first harmonic in-phase absorption CW spectrum for an ^{14}N spin-labeled 28-mer Duplex DNA in 50% sucrose at two temperatures (right). All samples described here were in PNE buffer (10 mM sodium phosphate pH 7, 0.1 mM EDTA, and 0.1 mM NaCl). The end-over-end tumbling correlation times of the DNA from hydrodynamic theory are presented for reference [35]. The spin–lattice relaxation rates are given in the figure legend. The left panel shows the^{14}N nitroxide dCTPO in 100% glycerol, at two temperatures, with isotropic rotational correlation times indicated. The spin lattice relaxation rates for dCTPO are found in Fig. 10 (top). The model nitroxide is provided to illustrate how the central ^{14}N feature (labeled A, top left spectrum) becomes an ambiguous measure of the peak-to-peak height and linewidth of the CW spectrum due to the structure that emerges as the motion is slowed (bottom spectrum). The peak-to-peak height and width are necessary for application of the CW power saturation method, and as illustrated, become untenable as a simple measures for the application of Eqs. (1) and (3) and when in the correlation time range of spin-labeled macromolecules typified by DNA. However, the low field feature (labeled B) retains a simple structure in this slower motion regime (as seen in all panels).

Fig. 17 shows an application of the CW power saturation method to the low field feature for ^{15}N 50-mer duplex DNA in 50% sucrose at 20 °C. The linear CW spectrum is shown in the top panel, and the CW power saturation rollover for the low field feature is shown in the bottom panel. The fit of Eq. (1) to the CW power saturation data is shown as a solid line, and the resulting ε and P_2 values are given in the figure legend. The value of R_1 from pSR on the low field feature is given in Gauss for comparison. A 1 Gauss value of R_2 is found from the low field feature CW spectrum, assuming it has a Lorentizan lineshape.

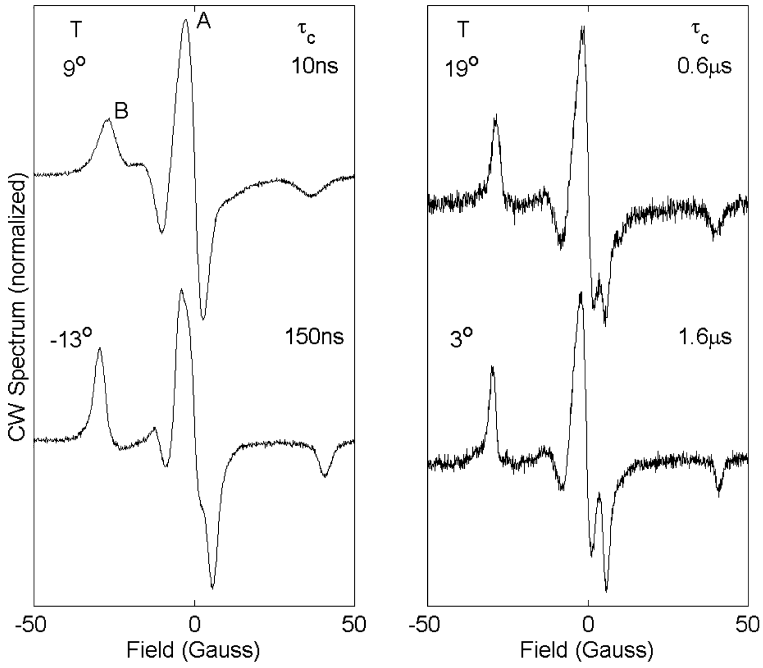

Fig. 16. (left) 0.1 mM [^{14}N]dCTPO in 100% glycerol at two temperatures. The labels A and B on the top spectrum indicate spectral features that are potential candidates for application of the power saturation method. The bottom spectrum shows how the spectral feature labeled A will exhibit structure for larger correlation times. The R_1 relaxation rates corresponding to these samples may be found in Fig. 10 (top). (right) ^{14}N spin-labeled 28-mer duplex DNA in 50% sucrose (deoxygenated) at two temperatures (nucleotide sequence is given elsewhere [35]). The spin-label is rigidly incorporated into the DNA backbone [4]. The correlation time reported is the global uniform end-over-end tumbling rate [35]. R_1 rates corresponding to these samples were measured with the observe frequency at equivalent positions within the center or low field manifold and gave 0.1171(4) and 0.0916(3) Mrad/s for 19 and 3 °C, respectively, with no dependence on nuclear manifold.

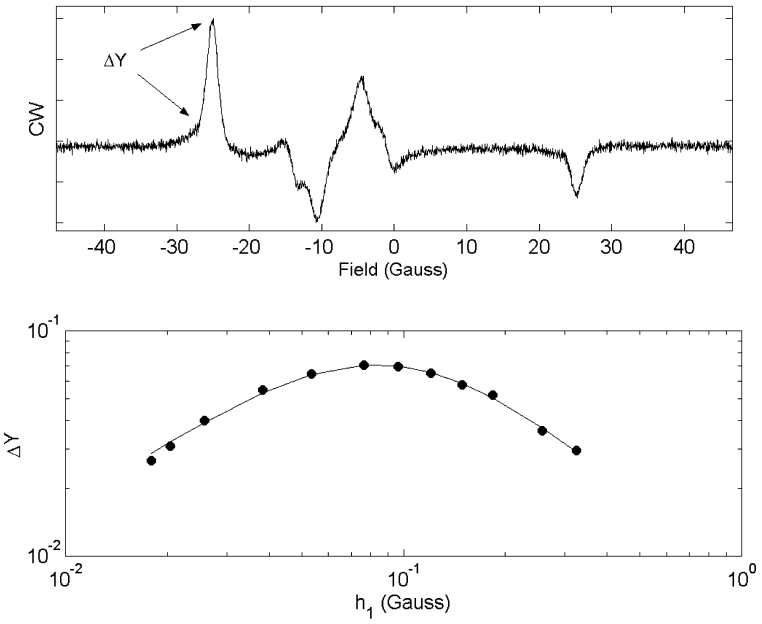

Fig. 17. ^{15}N middle labeled 50-mer duplex DNA in 50% sucrose (deoxygenated) at 20 °C (nucleotide sequence from [35]). (top) Linear CW spectrum, ΔY indicates the spectra feature used for power saturation analysis. (bottom) ΔY for low field feature (circles) as a function of microwave amplitude h_1. The solid line is the optimal fit to Eq. (1) : $\varepsilon = 1.13(3)$ and $P_2 = 0.0086(6)$ Gauss^2. R_1 was measured with the observing frequency on the low field feature and is 0.121(2) Mrad/s or 0.0069(1) Gauss.

The powder pattern (low temperature) CW spectrum of this sample is optimally fit with an intrinsic homogenous (Lorentzian) linewidth of 0.87 Gauss, and an inhomogeneous (Gaussian) component of 0.7 Gauss [5]. The ratio P_2/R_1 (from Fig. 17) predicts an R_2 value of 1.25(9) Gauss (see Eq. (1)).

Fig. 18 illustrates how R_1 from pSR varies as a function of dynamics for spin-labeled 50-mer duplex DNA in 0 and 50% sucrose. The top panel shows the linear CW spectrum at room temperature with the two sucrose concentrations. The middle panel gives the pSR spectra from the low field feature, where the signal is

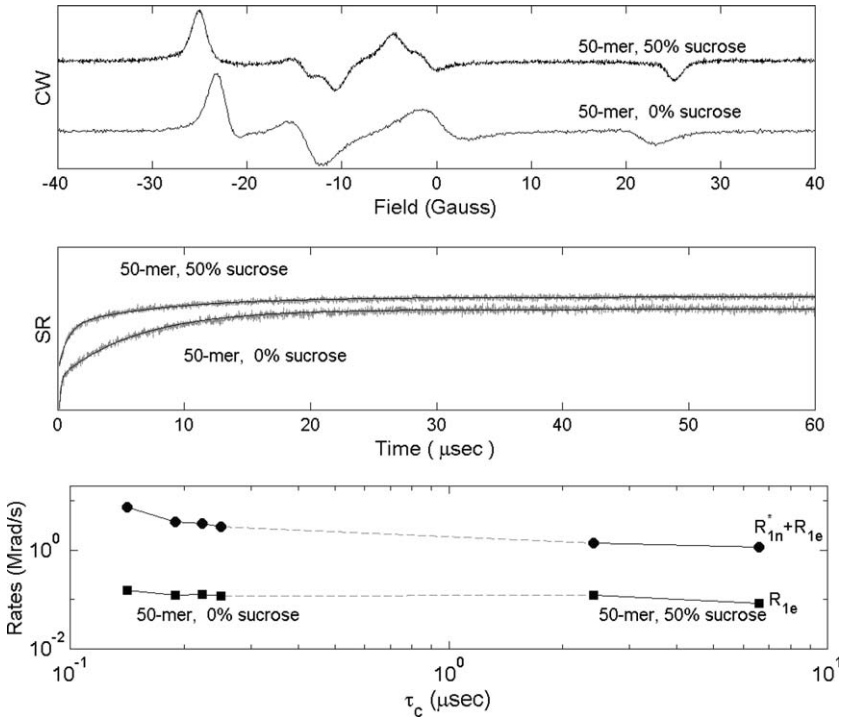

Fig. 18. Two ^{15}N middle labeled 50-mer duplex DNA's in 0% sucrose and 50% sucrose (deoxygenated) at several temperatures (nucleotide sequence give elsewhere [35]). (top) Normalized linear CW spectra at 20 °C. (middle) pSR signals at 20 °C with observing frequency on the low field feature (y-axis units arbitrary). Solid line is a fit using two exponentials. 0% sucrose signal is offset on the y-axis for visualization. (bottom) The slowest two relaxation rates, R_1 and R^*_{1n} for 0 and 50% sucrose as a function temperature, converted to the longest (end-over-end tumbling) correlation time according to a model of global DNA dynamics [35]. Connecting lines are for visualization.

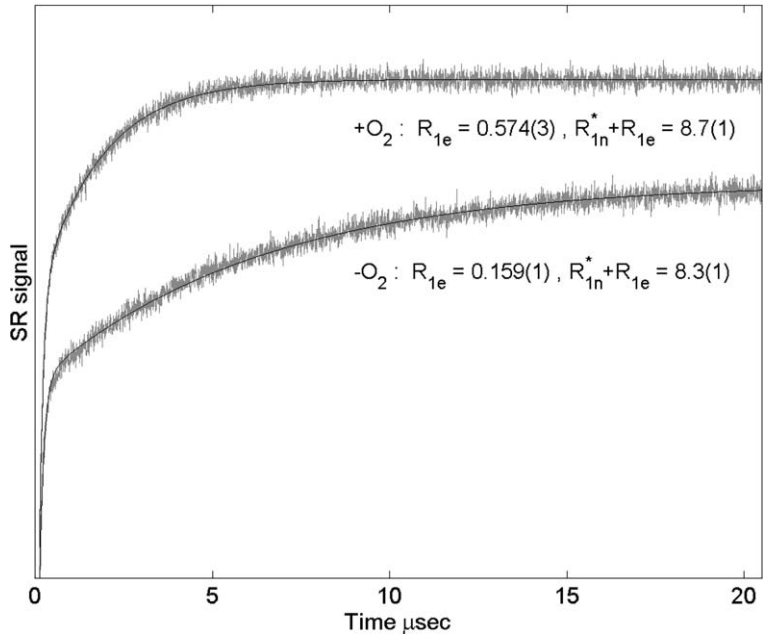

Fig. 19. SR spectrum with and without O_2 for the ^{15}N spin-labeled 50-mer duplex DNA in 0% sucrose at 20 °C shown in Fig. 18. Solid line is a two exponential fit to include the R_{1n} rate. The recovery signal without O_2 (i.e., $-O_2$) has been offset on y-axis for visualization.

largest. A nitrogen nuclear relaxation rate (R_{1n}) becomes necessary in fitting the pSR spectrum in this dynamical regime [13], and is shown along with the measured R_1 values in the bottom panel. The second exponential rate, which includes R_{1n}, is clearly visible in the pSR spectra as a fast initial rate (middle panel).

Fig. 19 shows the 0% sucrose 50-mer DNA pSR spectrum from the low field spectral feature with and without oxygen (air) at 20 °C. The collisional relaxation due to oxygen is given by the ΔR_1 shift, and is 0.415(3) Mrad/s.

4. Discussion

The three principal systems studied herein—^{14}N TEMPOL, sl-hGIIA $sPLA_2$, and sl-50 and 28-mer duplex DNA—indicate the practical issues involved in extracting relaxation rate information using either TD or CW techniques within the fast, intermediate, and slow motion EPR regimes, respectively, under conditions typical to biological applications. We now consider the difficulties of data analysis in each of the motional regimes.

4.1. Fast motion

Fast motion on the *X*-band EPR timescale is defined by correlation times smaller than 0.1 ns, and is characterized by motional narrowing of resonance lines. The method of simulation of linear CW spectra within the fast motion regime is well established [12]. Microwave power saturation effects have been accounted for theoretically, although fitting of detailed simulations to the full experimental CW spectrum under saturating conditions has not been implemented extensively [53–56]. We were motivated to simulate fast motion spectra to test whether the first 8 CW signals of the protonated nitroxide TEMPOL, undergoing fast motion, could be fit simultaneously as a function of the partially saturating microwave field to obtain consistent values of the R_1 and R_2 relaxation rates (see Table 1, Figs. 2 and 3). Conventional CW EPR spectrometers acquire only a single signal, which has inhibited simultaneous acquisition and fitting of larger sets of signals. Thus, this approach to fitting is unique in the MR literature in its inclusion of 8 CW spectra at each microwave power including: first and second harmonic, absorption and dispersion, in-phase and quadrature signals.

A fitting model that included the resolved SHF proton and carbon 13 structure was essential for accurate simulation of all spectra (see Figs. 2, 3, and Table 1). Excellent fits were obtained with χ^2's that for the most part did not exceed 5 and never exceed 10 [57]. The first harmonic absorption and dispersion showed increasing χ^2 with microwave power. The absorption χ^2 had a linear appearance as a function of microwave amplitude (in Gauss), and varied approximately as $\chi^2 = 16 \cdot h_1 + 1$. The dispersion χ^2 had a steeper initial slope, but leveled off at a χ^2 value of approximately 7. Increasing dispersion source noise at higher powers influences the noise present in the dispersion signal and acts to level off χ^2 for the dispersion signal. A possible reason for the microwave power dependence of χ^2 is the inclusion of only the central ^{14}N manifold in the fitting. The two other nitrogen hyperfine lines approximately 17 Gauss distant from the center manifold were excluded. The tails of these omitted spectral lines overlap the center manifold as power broadens the homogenous linewidths. In addition, a subtle instrumental artifact arising from resonance-induced changes in the quality factor of the resonator can contribute to lineshape asymmetry. Such effects were not accounted for in the theoretical model. An apparently good fit with slightly worse χ^2 parameters was obtainable with a second incomplete model containing two sets of six methyl protons (6 equatorial with 0.49 Gauss splitting and 6 axial with 0.06 Gauss), and one set of two ring protons (0.32 Gauss for the presumed equatorial protons). This second incomplete model lacks the single ring proton at the 4-position; the absence of this single proton splitting in the second model results in an even number of proton hyperfine lines. The absorption first harmonic χ^2 dependence on microwave power, for the incomplete model, began near 1 and increased with a slope of 26 χ^2 units per Gauss (a factor of 1.6 larger than the more exact model). The results of fitting to this incomplete model are significant because they illustrate the sensitivity in fitting the SHF, and show the concomitant necessity of having saturated absorption, dispersion, and quadrature signals to uniquely determine the proper SHF model and the relaxation rates. For the incomplete model, the spin–lattice relaxation rate, R_1, obtained was similar to that reported in Table 1, but the R_2 was nearly two fold larger. Two factors distinguished the better model of the SHF structure. For the fitting depicted in Figs. 2, 3, and Table 1, the relative amplitude of absorption and dispersion was constrained to be that predicted by the lineshape model function (see Section 2). In contrast, the incomplete model could not be fit without allowing separate scaling values on the absorption and dispersion predictions. While the absorption and dispersion amplitudes floated to nearly equal values at low powers in the incomplete model, they diverged under saturation wherein the experimental first harmonic in-phase dispersion spectra were smaller than model predictions by up to a factor of 2. The second indication of the failure of this incomplete model was its prediction of greater resolution of SHF structure in the first harmonic quadrature dispersion than was actually observable in the data. Both of these failings are explained in the context of the fitting results of the full model of SHF structure. The inherent linewidth that

was found to be optimal in the complete model of SHF was twofold smaller, and thus saturated earlier (at lower microwave powers). The second harmonic in-phase signals have greater resolution of SHF structure than their first harmonic counterparts (see Fig. 3 left vs. Fig. 2 left), but did not serve as a clear aid in distinguishing the two models of SHF structure presented. The important features which allowed these two models of SHF to be distinguished were: (1) constraining the fit at all levels of saturation such that the absorption/dispersion amplitudes are the literal prediction of the lineshape model, and (2) the inclusion of out of phase first harmonic dispersion. Low microwave power data alone were not sufficient to clearly distinguish between these two SHF models. SHF values similar to those found here (Table 1) have been previously reported [24]. Previous estimates of SHF values were obtained for the low power first harmonic in-phase absorption spectrum of TEMPOL by iterative simulation and visual comparison, and were guided by NMR-measured hyperfine coupling constants and previous EPR refinements. The linewidth used in that study was greater by a factor of 2 than that reported here (Table 1). The example provided in that work to illustrate the quality of fit was visibly worse than that attained here, although no quantitative measure of the quality of fit, such as χ^2, was provided.

The values of R_1 and R_2 can be calculated from fast motion theory by including the relaxation mechanisms of spin–rotation, electron–nuclear dipolar interaction, and spin diffusion [13,58]. The rates with these mechanisms, using the known A and G tensors of TEMPOL, are 50 mG and 80 mG for the spin–lattice and spin–spin relaxation rates respectively at 20 °C and assuming a reorientation correlation time of 30 ps [13,59]. Approximately 40 mG should be added to these rates due to collisional nitroxide–nitroxide Heisenberg exchange at the 0.25 mM concentrations used here [23]. The inclusion of collisional broadening brings the theoretical estimates near to the values determined by experiment (Table 1).

The presence of resolved, or partially resolved, SHF interactions can have a profound influence on the ability to extract meaningful relaxation parameters. The fitting performed here demonstrated that it is essential to have a complete model of the SHF structure, and to have both first harmonic dispersion components in addition to the standard absorption component to obtain unambiguous results. This procedure is elaborate by comparison to the CW power saturation method of Eq. (1). Fitting the "rollover" of the largest peak-to-peak height of the standard absorption signal of TEMPOL (e.g., Fig. 2, left top) gave an erroneously broad "rollover" curve, with an ε less than 1, in contrast to the value of 3/2 expected for a homogeneously broadened line [41]. The P_2 value obtained by the CW saturation method was 20% larger than the product of R_1 and R_2 from Table 1. Furthermore, a discontinuity in the slope of the rollover curve is perceptible within the high power ($h_1 > 0.5$ Gauss) region of the curve. A single curvature parameter ε fails to describe this bifurcation of power dependence. Eq. (1) fails as a functional form because the "rollover" is a composite of $\varepsilon < 1$ dependence at low microwave powers, and $\varepsilon = 3/2$ at higher powers. Both the experimental and simulated data show that P_2 values obtained by fitting lineshapes to Eq. (1) have limited meaning when SHF is resolved at the level seen in Fig. 2.

SHF structure is not generally resolved in standard spin labeling experiments in most biological applications. Three sources can obscure the presence of SHF structure in the linear CW spectrum: (1) dynamics, which are often a complicated superposition of global and local motions, (2) over-modulation, and (3) collision-induced broadening. To first order, dynamics broaden the homogeneous lines, and decrease the ratio of SHF splitting to linewidth. This makes the replacement of SHF structure by a residual Gaussian convolution increasingly reasonable. The same is true for collision-induced broadening. These cases may be contrasted with the effects of Zeeman over-modulation on apparent linewidth. Since it is standard practice to overmodulate in biological applications for increased signal-to-noise, we comment on the effect of modulation here.

Zeeman modulation distorts a homogenous (Lorentzian) lineshape such that even in the low microwave amplitude regime the lineshape is no longer Lorentzian in form. An analytical expression for a modulated Lorentzian lineshape that includes the effect of saturation can be derived from the Bloch equation in the low modulation frequency limit [23,37,60,61]. A closed form expression for the "rollover" function (that replaces Eq. (1)) can be derived from the modulated lineshape. The "rollover" function has a more complicated form than Eq. (1) and is not obtained by a simple broadening of the spin–spin relaxation rate. In other words, there is no simple generalization of the P_2 and ε parameters to rigorously account for the effect of over-modulation. A less precise definition of P_2 allows for rough comparison with Eq. (1). The maximum ΔY as function of the microwave amplitude, from Eq. (1), is $(\gamma h_1|_{\mathrm{Max}\,\Delta Y})^2 = R_1 \cdot R_2/2 = P_2/2$ when $\varepsilon = 3/2$ [40]. The effective $P_{2,\mathrm{eff}}$ in the presence of over-modulation, obtained by locating the maximum of the "rollover" function, which takes into account modulation, is:

$$P_{2,\mathrm{eff}} = R_1 \cdot R_2 \cdot 4 \cdot \left(1 + \frac{3 \cdot R_2}{\sqrt{R_2^2 + (\gamma h_{\mathrm{m}}/2)^2}}\right)^{-1}, \qquad (9)$$

where γh_{m} is the peak-to-peak modulation amplitude [61]. Modulation, therefore, increases the effective value of the "rollover" parameter P_2 by up to a factor of four. Furthermore, if the peak-to-peak height of an

over-modulated single resonance lineshape is fit to Eq. (1) as a function of microwave amplitude an effective ε will arise. Attenuation of the signal peak-to-peak height in the pre-saturation region due to over-modulation causes the "rollover" curve to broaden (lower ε). When a set of SHF lines is over modulated, a similar trend is observed: the predicted ε is decreased, and the predicted P_2 value is increased. Therefore, while over-modulation may smooth out SHF structure in a CW spectrum and give the appearance of a single resonance line, over-modulation leads to erroneously high P_2 values when analyzed by the saturation rollover method embodied in Eq. (1). In part, to avoid this problem, Marsh and coworkers proposed the use of the saturated double integral of the first harmonic CW spectrum in place of the conventional derivative signal to obtain the value of $R_1 \cdot R_2$ because of the double integral's simple relation to the modulation amplitude [54,60,61]. However, the double integral method is difficult to implement experimentally because breadth and consistency of baseline are important for accurate double integral measurements. We find that baseline consistency can be problematic for low concentration samples encountered in biological contexts. Therefore, we have investigated the prospects offered by TD pulsed techniques as an alternative to CW methods to obtain meaningful information on relaxant effects in biological systems. Protonated TEMPOL in water at room temperature represents an extreme in which SHF structure is resolved.

The presence of SHF leads to a superposition of off-resonant effects in TD signals. Each SHF frequency-field position contributes to the FID spectrum. The relative significance of each SHF line is determined by: (1) CW amplitude (Fig. 4, top), (2) the degree of offset from the center of the pump pulse frequency-field position, and (3) the pulse duration and power. Simulation of the effect of the pump-pulse duration was accounted for by two approaches. The first approach, used for the simulations shown in Figs. 4–7, consisted of treating the pump pulse as a pure frequency that persists for the pump time τ_p. The "spectral width" of the pump pulse arises internally within the solution of the Bloch equations because off resonant lines are driven less efficiently than those near resonance. For example, the magnetization induced in the $x-y$ plane following a pulse of duration τ_p for a single resonance line in the limit of vanishing linewidth is given by the standard windowing function:

$$M_y(\Delta) \propto h_1 \cdot \sin\left(\sqrt{h_1^2+\Delta^2}\cdot\tau_p\right)\Big/\sqrt{h_1^2+\Delta^2}, \qquad (10)$$

where Δ is the offset of the resonance position from the pump frequency, and h_1 is the pump microwave amplitude (expressed in frequency units) [62]. An alternative, but approximate, approach is to assume, a priori, a frequency distribution for the pump pulse. This distribution function is the Fourier transform of the TD profile of the pump pulse. With this scheme the Bloch equations are solved using the pump power delivered at the specific frequency of the resonance line with amplitude determined by the pump frequency distribution. This method of simulation gave results similar those found in Figs. 4–7, under the assumption of a square frequency distribution of width $1/\tau_p$.

For typical pulse widths on the order of 1–2 Gauss, much of the SHF structure is stimulated. The FID is comprised of damped oscillations whose frequencies are due to the resonance offsets comprising the SHF structure. The constructive interference of these oscillations results in an echo-like phenomena, which is superposed on the fundamental signal that decays with rate R_2 (see Figs. 4 and 5 as well as Eq. (5)). This echo is not the same as the refocusing phenomena encountered in an electron spin echo (ESE) experiment, but is due to the independent multi-harmonic coherent evolution of the SHF resonance conditions. The shoulder of the first SHF echo directly competes, in the present case, with the R_2 decay. This can make the FID difficult to analyze for R_2 information. The simulations of the FID shown in Figs. 4 and 5 were carried out with no adjustable parameters, using only the CW-determined rates (Table 1), and the experimental pump time, power and frequency offsets. The early time behavior of the FID (first 0.2 μs) seen in spectrum (a) of Fig. 4 results from subtle superposition of off resonant contributions that are not captured by the simple 7 line SHF model, spectrum (b) of Fig. 4. These early features are sensitive to pulse characteristics, and are seen most dramatically for the pulse conditions in Fig. 5. The simple expression for the FID given by Eq. (5) indicates that the R_2 rate information is contained in the relative amplitudes of the FID coherent "echoes" existing at time points $t = n \cdot 2\pi/\bar{a}$. The echoes are modulated by resonance offset from the center of the SHF manifold as seen in Fig. 5. To accurately simulate the experimental FID spectrum the full SHF pattern, comprising some 3000 resonances, (obtained from detailed CW fitting, Table 1) was necessary (Fig. 4). Electron spin echo (ESE) measurements of R_2 are available in the fast motion regime, and are an attractive alternative for SHF independent determination of R_2 [63]. For example, the R_2 has been measured for the ketone analog of deuterated TEMPOL in toluene-d_8 for a temperature range that covers fast motion [64]. The value of R_2 given in this reference for the viscosity point corresponding to water at room temperature is 70 mG, and was extrapolated to zero spin concentration by the authors. Our values of R_2 from CW fitting of protonated TEMPOL (137.3(3) mG, see Table 1) and from the FID of deuterated TEMPOL (127(1) mG, Fig. 8) are in reasonable agreement with this the ESE result when collisional broadening at the 0.25 mM concentrations used is included [23].

The SHF off-resonance effects are less obvious in the pSR signal because they enter through a FID-type component, which depends on R_2. Much of this R_2 dependent contribution can be cancelled by random pump-observer phase, and appropriate pump time and pump power conditions [14,65,66]. To minimize the influence of the remaining FID-like transient, fitting to the "tail" of the pSR spectrum has been prescribed [14]. Fitting the pSR spectrum of TEMPOL under a π pulse of $\sim$2 Gauss width to a simple single exponential, after cropping the first 0.5 μs, resulted in an effective R_1 rate that was 20% larger than the R_1 rate found from fitting of the CW spectra (Table 1, and Fig. 6). This discrepancy led us to investigate the sensitivity of the effective R_1 rate to the presence of SHF. The dependence of the effective R_1 rate on inverse pump time $1/\tau_p$ was investigated by fitting a series of pSR spectra acquired with different pump times to a simple exponential after cropping the first 0.5 μs (Fig. 7). The excitation pulse with longest pump time has the narrowest width, and, therefore, should stimulate fewer of the SHF lines. Fig. 7 illustrates the trend found both experimentally, and theoretically. When a long pump time is used (10 μs), the measured R_1 rate approaches within 5% of the value determined above by the CW techniques. In contrast to the long pulse limit, the experimentally determined R_1 rates show a maximum at $1/\tau_p \approx 1.2$ MHz. The pump times near the maximum corresponds to pulse widths that just encompass the first envelope of SHF splitting at $\sim$0.45 Gauss (see Table 1). The contribution from resonance positions at the $\sim$0.45 Gauss SHF splitting results in off resonance contributions to the pSR spectrum through the residual FID-like component present in the pSR signal. The off resonance contributions are manifested, in analogy to a conventional FID, as a damped oscillation with a period of $\sim 0.8\,\mu s = 1/(2.8\ (\mathrm{MHz/Gauss}) \cdot 0.45\ (\mathrm{Gauss}))$. This SHF artifact interferes with the $\sim 0.63\mu s = 1/(1.6\ \mathrm{Mrad/s}\ )$ fundamental $T_1 = R_1^{-1}$ (Table 1) exponential decay. The first cycle of the 0.8 μs oscillation appears as an effective shortening of the T_1. Because the amplitude of the SHF oscillation is governed by R_2, cropping the pSR spectrum at several T_2 time constants is preferable. In the present case, however, R_1 and R_2 are not timescale separated (see Table 1).

The effective spin–lattice relaxation rate in the presence of oxygen was obtained with a pulse time of 170 ns, by cropping the pSR spectrum at 0.5 μs (Fig. 7 legend) and fitting to a single exponential rate. The oxygenated pSR spectrum was simulated with a model that included the SHF structure (the same method as in the deoxygenated case), but with 2 Mrad/s added to the basic relaxation rates. The 2 Mrad/s collisional relaxation rate of oxygen was estimated independently from deuterated TEMPOL (see Fig. 8). The theoretical effective rate was obtained by cropping the simulation in the same manner as the experimental data, and gave a value of $R_{1\mathrm{eff}}^{+O_2}$ that was within 5% of the experimental oxygenated effective rate (Fig. 7, legend). The value of $\Delta R_{1\mathrm{eff}} = R_{1\mathrm{eff}}^{+O_2} - R_{1\mathrm{eff}}^{-O_2}$ for the 170 ns pump time data is 78% of the expected 2 Mrad/s change. The collisional relaxation rate obtained from the effective spin–lattice relaxation rates does not faithfully reflect the true change in relaxation rates, because SHF structure obscures the true rates. Therefore, caution should be exercised in using the effective oxygenated and deoxygenated R_1 rates from pSR for short pulse conditions to asses collisional relaxation.

In summary, a pSR spectrum is seen to retain much of its exponential character, and can reflect the intrinsic spin–lattice relaxation rate under appropriate (long) pulse conditions. The influence of pulse length on the effective spin–lattice relaxation rate has been realized in applied studies using pSR because the length of the pump pulse influences the relative amplitudes of the R_2 dependent FID-type term, as well as the decay containing the spin-nuclear rate [14,67]. The investigation here stresses the importance of a long pump pulse to minimize the effect of SHF structure. This aspect of the dependence of effective R_1 rate on pulse length has not been experimentally or theoretically investigated in detail. The nearly exponential appearance of the pSR spectrum under moderate pulse length conditions can lead to error in interpretation of the spin–lattice relaxation rate, due to SHF structure. The influence of SHF structure in the pSR spectrum is to be contrasted with the FID, whose R_2 rate dependence is clearly obscured (Figs. 4 and 5 vs. Fig. 6). Care should be taken over and above the issue of SHF structure in strict interpretation of the pSR spectrum as a single exponential in the fast motion limit due to the importance of spin-nuclear (R_{1n}) processes that are competitive with the R_1 rate, especially in the early time portion of the spectrum [13]. The discussion here of protonated TEMPOL should be contrasted with deuterated TEMPOL. In the deuterated nitroxide the splitting of the SHF lines are well within the homogenous linewidth. Consequently, SHF structure influences both the FID and pSR signals at all pump times.

In the case of deuterated TEMPOL SHF structure is not resolved in the CW spectrum, or the FID. The SHF structure of the CW spectrum may be reasonably well accounted for as a convolution of a Lorentizian lineshape with a Gaussian distribution representing the SHF distribution [44]. In the time domain this results in the product of an exponential and a Gaussian decay (Eq. (6)), by the Fourier convolution theorem. Short pump pulses allow the entire SHF envelope to be probed. The spectra are then analyzed by Eq. (6) to quantitatively fit and remove the SHF effect (see Fig. 8). The analog of Eq. (6) for finite pulse widths is complicated, and never limits to an SHF-free expression [61]. Therefore, long pulses in experiments will not give relaxation rates that are free of SHF effects.

Upon addition of O_2 the exponential rate obtained from the FID spectrum of dTEMPOL is increase two-fold, while the Gaussian component is unaffected (see Fig. 8, legend). The oxygen relaxation observed here is identical within error to that obtained for deuterated TEMPONE by accurate linewidth simulation [68]. The presence of the Gaussian contribution in the FID is evident when contrasted with a fit of the FID to a single exponential rate (dashed lines, Fig. 8). It is noteworthy that, like the echo seen in the protonated case, this Gaussian functional form implies an absolute timescale for the decay spectrum (unlike a pure exponential decay). In this case, time translation does not result in merely a scaling of the spectrum. The Gaussian and Lorentizan components from the FID (Fig. 8, legend) may be combined using Lebedev's formula to give an effective peak-to-peak CW linewidth of 0.47 Gauss without O_2, and 0.56 Gauss with O_2 [44]. These values agree with the observed CW peak-to-peak linewidths (not shown). The intrinsic R_2 (without oxygen) from the FID (Fig. 8, legend) is within 8% of the R_2 found for protonated TEMPOL (Table 1) at the same nitroxide concentration, representing good agreement. In principle, the R_2 rate for protonated TEMPOL could contain a relaxation contribution from methyl protons as a dynamic modulation of the electron-nuclear interaction [69]. Deuterated TEMPOL would then be expected to have a smaller R_2 relaxation rate than the protonated nitroxide, due to the fact that the gyromagnetic ratio of the deuteron is smaller than the proton by a factor of 6.5. The correlation time for methyl rotation does have significant overlap with the electron Larmor frequency at room temperature, assuming an activation barrier for methyl rotation on the order of kT, and has been the basis for analysis of the spin–lattice relaxation rates of the ketone analog of TEMPOL in 1:1 H_2O/Glycerol solutions [70]. The question of a possible contribution to spin–spin interactions from dynamic modulation of methyl protons remains open in the fast motion limit.

The pSR and pELDOR spectra of deuterated TEMPOL were fit with R_1 and $R_1 + R_{1n}$ rates of 1.03(2) and 2.59(7) Mrad/s, respectively (data not shown). This R_1 rate is 40% smaller than expected from the protonated data, and could be due to artifactual trade off between these two rates during fitting. Alternatively, there could be an H/D isotope effect, in principal, if dynamic modulation of methyl protons is a mechanism that contributes to spin–lattice relaxation in the fast motion limit. Additional data sets containing pSR spectra with large (saturating) observing microwave powers were acquired to exhibit Torrey oscillations. Inclusion of this additional data did not improve agreement, but indicated that a more detailed model of the R_{1n} mechanism was necessary for a complete fit (data not shown). Adding the ~2 Mrad/s collisional oxygen rate observed from the FID (Fig. 8) to the two rate model of low observe power pSR shows that a 2 Mrad/s collisional relaxation rate is consistent with the experimental oxygenated pSR data. Hyde et al. [17] have reported a ~1.25 Mrad/s collisional-induced relaxation rate change by O_2 for deuterated TEMPONE in water at room temperature. Elsewhere, the same authors attribute the apparent difference between oxygen collisional relaxation observed by CW linewidth studies vs. pSR to an inherent difference in collisional efficiency of O_2 for transverse vs. longitudinal relaxation rates [42].

The CW and TD data for protonated TEMPOL illustrate that resolved or partially resolved SHF structure must necessarily be included in the data analysis to extract accurate rates. CW and pulsed methods can and do agree when the model of the SHF structure is complete. To illustrate this we used the SHF pattern and relaxation rates found from fitting CW spectra to simulate the FID and pSR signals. The simulations were then compared with the experimental spectra. We found that the highly SHF-distorted FID spectra could be understood quantitatively in terms of a superposition of individual FID's from each of the SHF resonance positions. While the long-time behavior of pSR spectra appeared exponential the effective relaxation rate was strongly influenced by pulse conditions due to the SHF structure. The long time behavior of the pSR signal under a long microwave pulse gave an effective R_1 (Fig. 7) that was closest to the CW determined value (Table 1). While the simulation of the 8 principle CW spectra as a function of microwave power provided the most reliable method for extraction of rate information in the case of protonated TEMPOL, it also involved acquisition and fitting of a large data set to a detailed model.

The procedure for analyzing CW progressive saturation data exemplified by Eq. (1) has the potential for simplifying the CW analysis. We discussed the implications of SHF structure for this common mode of data analysis. Application of "rollover" analysis of CW power saturation data, as exemplified by Eq. (1), can result in erroneous estimates for the important parameter P_2. Furthermore, Zeeman over-modulation of the SHF manifold, while it leads to superficial smoothing of the SHF manifold, does not lead to any simplification of the power response of the CW spectrum. Indeed, over modulation leads to an ε parameter in Eq. (1) that is not a simple constant, but is now a function of the amount of microwave power.

Deuterated TEMPOL was also investigated. In contrast to the protonated nitroxide, short pulse conditions that stimulate the entire SHF envelope were preferred in the deuterated experiments. Because the SHF structure is composed of splittings that are with the homogenous linewidth, a simple Gaussian distribution for the short pulse experiments adequately modeled SHF structure in the FID and allowed for clean extraction of the R_2 rate.

4.2. Intermediate motion

Intermediate motion in *X*-band EPR is characterized by correlation times falling between 0.1 ns and 0.1 μs. In this regime, SHF structure is dynamically averaged, and is unresolved. The spin label's dynamics, when coupled by a flexible linkage to a biological molecule, are generally within the intermediate motion range of correlation times [1–3,10,46]. Two issues besides unresolved SHF structure interfere with the clean extraction of rate parameters in this regime. First, while the motional dependence of the spin–lattice relaxation rate is monotonic and well modeled as a function of correlation time [13], the R_2 relaxation rate is not as well characterized. The perturbation approach for calculating the relaxation rates in the fast motion regime breaks down for spin–spin processes in the so called Redfield catastrophe, predicting a perpetually increasing R_2 rate as a function of increasing correlation time [12,41]. Slow motion theory, which uses a stochastic Liouville equation to describe the effect of rotational diffusion on relaxation rates, may be used in the intermediate motion regime with a basic motion independent (intrinsic) R_2 rate added phenomenologically [41,71]. The predictions of the stochastic Liouivlle approach have not been tested by extensive fitting of the entire experimental saturated CW first harmonic absorption spectrum [72,73]. Experimentally, FID and ESE measurements are thwarted by the large magnitude of the effective spin–spin relaxation, but indicate that the R_2 rate peaks as a function of correlation time in the intermediate motion regime [63]. The second issue affecting quality of analysis is the fact that the spin-label motion is often a complex superposition of contributions from global molecular dynamics and local spin-label conformational dynamics. These complications are accounted for in fitting CW "rollover" data through the semi-empirical formula given by Eq. (1). The ε parameter is meant to subsume some of the effect of dynamics, whereas, the P_2 parameter is taken to represent the effective product of spin–spin and spin–lattice relaxation rates. The data for hGIIA $sPLA_2$ indicates two problems with the practical application of this formula: (1) a tradeoff in the roles of ε and P_2, and (2) the ambiguity of R_2 when extracting information from P_2. TD measurements of R_1 provide an independent standard by which the complications arising in the analysis of CW power saturation data may be judged.

TD and CW data are compared for both hGIIA $sPLA_2$ and the model spin-label dCTPO to illustrate the qualitatively different role of dynamics in the CW and TD measurements. The dCTPO spin-label is similar in structure to the commonly used MTSSL reagent used to spin-label proteins [1].

Fig. 9, left, illustrates the well-known sensitivity to dynamics of the linear first harmonic in-phase absorption signal within the intermediate motion regime. The right panel shows a set of CW spectra obtained within a typical protein spin-labeling experiment using the MTSSL label, and consists of spin-labeled protein that is bound to mixed micelles. The CW spectra reflect the existence of two classes of residues—protected and exposed—showing different apparent dynamics. For example, the centerlines of S35, S120, and T104, appear narrower than those of the set V3, L19, and F23 (see ΔH_{P-P} on right panel). The center peak-to-peak linewidth has been suggested as a semi-quantitative measure of local conformational spin label freedom [2,74]. Assigning a single correlation time to the hGIIA spectrum (Fig. 9, right) is difficult because the spectrum results from a superposition of global protein and local spin-label conformational dynamics. However, direct comparison with the isotropically moving model spin-label (left panel) implies an effective isotropic rotational correlation time of 1–3 ns for all of the spin labels attached to the protein (see τ_c labels in left panel).

Fig. 10 shows quantitatively, how the spin–lattice rate (R_1) depends on dynamics. The R_1 rates for the [^{14}N]dCTPO model nitroxide agree with those determined previously for an ^{15}N nitroxide (dTEMPOL) over the same correlation time range [13]. As the model spin-label data shows (Fig. 10, top), a monotonic dependence of the relaxation rate on correlation time is found. The TD R_1 rate in the intermediate motion regime is dominated by spin–rotation and spin-diffusion mechanisms and is decreasing with increasing correlation time [13]. The effect of SHF structure (discussed for fast motion above) is minimal because the R_2 relaxation rate for typical nitroxides is separated from R_1 by two orders of magnitude in the intermediate motion regime [41]. Thus the FID-like component of the pSR signal does not interfere with the spin–lattice relaxation rate. The functional form of the pSR spectrum remains exponential in time, with the possible inclusion of secondary much faster (R_{1n} containing) spin-nuclear rates. The R_{1n} rates are an order of magnitude larger than the spin–lattice relaxation rate R_1, for this range of correlation times, and may often be neglected in practice [13]. The simple form of the pSR spectrum is to be contrasted with the large qualitative changes found in linear CW spectra (Fig. 9 left panel). In the CW power saturation technique the CW functional form is only semi-empirically accounted for by the ε parameter of Eq. (1) used to fit peak-to-peak rollover data. While the effect of dynamics on the value of the ε parameter has been theoretically investigated in the intermediate motion regime, the possible influence of unresolved SHF structure on this parameter has not been assessed in the same manner and awaits further investigation [41].

The bottom panel of Fig. 10 illustrates the motional dependence of the R_1 rate from pSR on the spin-labeled hGIIA enzyme for the same spin labeling positions whose CW spectra were shown in Fig. 9. The variation

of the pSR measured R_1 values is correlated with the variation in mobility implied by the CW spectra given in Fig. 9, as well as the accessibility to solvent phase as determined by CROX/NiEDDA relaxation studies [21,34]. The values of the peak-to-peak linewidth from the CW spectrum (Fig. 9, right) are linearly correlated with the R_1 values (Fig. 10 bottom and Table 2, column 8). Amongst the data presented here, for hGIIA bound to micelles (Fig. 9 and Table 2), the CW linewidth and R_1 values both vary by a factor of 2 from the most immobilized (F23) to most mobile (S35) example. The CW and TD data therefore exhibit the same sensitivity to dynamics. The peak-to-peak linewidth of the CW spectrum is directly related to the underlying spin–spin relaxation rate, R_2, in the fast motion regime, and has a know dependence on isotropic rotational correlation time [12]. The CW spectra shown in Fig. 9, as examples of intermediate motion, approach a motional regime where the simple peak-to-peak linewidth is expected to fail as a reflection of the underlying R_2 relaxation rate because R_2 begins to exceed the measured linewidth [41]. In addition, as the slow motion limit is approached a simple peak-to-peak distance is no longer present in the spectral lineshape (see Fig. 16). In contrast TD pSR spectra retain an exponential form over the entire intermediate to slow motion regimes, and the dependence of R_1 on correlation time remains monotonic (see Fig. 10, top and slow motion discussion below). This makes the R_1 relaxation rate, as measured by pSR, an attractive experimental measure of dynamics.

The R_1 values for the spin-labeled protein exhibited in Fig. 10 are larger than expected from the isotropically moving model nitroxide measurements when the molecular correlation times are inferred by comparing the appearance of the CW spectra (right vs. left panels of Fig. 9). The CW spectrum of the spin-labeled enzyme reflects both fast (anisotropic) spin-label conformational dynamics due to local steric confinement of the spin-label linkage, as well as the slower global dynamics of the entire protein [74]. The spectral averaging, which is due to the protein's global orientational dynamics, causes the CW spectrum to appear slower-moving than the actual timescale of local anisotropic spin-label dynamics. The exponential saturation recovery spectra are dominated by the faster rate components, which correspond to the fast local dynamics. This sensitivity of pSR to local dynamics provides a potential means of deconvolving global and local motions. The degree to which the specific spin-label used here (MTSSL) reflects the local protein back-bone motion is currently being pursued by CW EPR [74]. pSR on spin-labeled DNA, using a rigidly incorporated probe, is discussed below and also shows sensitivity to local motion.

Collisional relaxation studies offer an alternative means of comparing TD and CW. We exhibit the collisional relaxation of the spin-labeled hGIIA enzyme by O_2, both in solution and bound to vesicles (see Section 2). The relaxation by O_2 observed is small compared to the spin–spin relaxation rate, as may be seen by the absence of detectable broadening in the CW spectrum. The approximations of Eq. (2) therefore apply. Fig. 11 illustrates how extraction of the CW P_2 parameter, using Eq. (1), may be compromised by artificial tradeoff with the ε parameter, under conditions typical to biological experiments. In addition to this systematic error, Fig. 11 also illustrates the inherent relative error of the CW vs. TD measurements. In principle the R_2^0 dependence of ΔP_2 should be cancelled by the ratio $\Delta P_2/P_2^0$, where $P_2^0 = P_2^{-O_2}$, leaving an expression equivalent to the TD measured quantity $\Delta R_1/R_1^0$ (see Eq. (3)). The CW fractional change has the advantage that $\Delta P_2/P_2^0 = (P_2^{+O_2} - P_2^{-O_2})/P_2^{-O_2}$ is independent of the resonator-dependent calibration parameter α (see Eq. (1)). $\Delta P_2/P_2^0$ also tests the R_1 dependence of P_2 using only 'rollover'-determined parameters. Experimentally, the linearly related parameter $P_2^{+O_2}/P_2^{-O_2}$ has been interpreted by Popp and Hyde as a semi-quantitative measure of oxygen relaxivity [75,76]. Fig. 11 shows $\Delta R_1/R_1^0$ plotted vs. $\Delta P_2/P_2^0$ to illustrate whether the two measurements are truly similar. Solid lines represent complete correlation. The *Y*-axis of the left panel in Fig. 11 illustrates the fractional change in P_2 as a result of oxygen exposure for the hGIIA $sPLA_2$ enzyme in solution with no membrane substrate. The *X*-axis of the left panel is the quantity $\Delta R_1/R_1^0$, under the same conditions. The right figure shows the same TD data, but with the CW data analyzed by a more restrictive procedure. In using Eq. (1) artifactual tradeoff can easily occur between the ε and P_2 parameters, as both affect the position of the "rollover" maximum. To introduce internal consistency and minimize the potential for this artifactual tradeoff, the CW rollover data was fit to the same ε parameter for both $\pm O_2$ conditions. Since the P_2 values for both conditions are linked to the same ε, individual P_2 tradeoff with ε is moderated. This seems to be an improved prescription to obtain accurate P_2 values, as discussed below.

The correlation coefficient (R^2) for the CW and TD data is 0.63 in the right panel of Fig. 11. The R^2 for the left panel is 0.002, indicating no correlation. The trend lines given in the figures illustrate the ideal of complete correlation. Sites 3, 70, and 115 in the left panel are outliers. If labeling sites 3, 70, and 115 are excluded, the R^2 is 0.79 for the left panel. Exclusion of these residues in the right panel results in an improved R^2 of 0.80, but this result is principally influenced by the presence or absence of residue 3 alone. No reason exists to exclude any data. Therefore, the conclusion is that fixing ε to be the same for both $\pm O_2$ conditions leads to greater consistency with the TD measured data. However, the CW fractional changes in the right panel are displaced by a constant amount relative to the TD values.

A dashed line represents the best fit to the data, assuming a one-to-one slope. The values of $\Delta P_2/P_2^0$ are 30% larger, on average, than those predicted by TD rates in the right panel. The effect of the ε constraint is to shift both $P_2^{+O_2}$ and $P_2^{-O_2}$ by moderate amounts (see Section 3 and Tables 2, 4), so the effect on the value of $\Delta P_2/P_2^0$ cannot be isolated to a single factor.

The CW factional change $\Delta P_2/P_2^0$ is useful for comparison with TD, but ΔP_2 is the quantity of experimental interest because of its relation to the product $\chi \cdot [O_2]$ (see Eq. (2)). In practice the R_2^0 dependence of ΔP_2 is minimized by dividing ΔP_2 by the experimental CW peak-to-peak linewidth, as an independent measure of R_2^0 [11]. Fig. 12 shows the results of this procedure applied to the hGIIA $sPLA_2$ enzyme data. The left panel shows $\Delta P_2/R_2^0$ plotted against the ΔR_1, for the case of enzyme free in solution with no membrane substrate. The left panel of Fig. 12 shows that $\Delta P_2/R_2$ over-estimates the TD measured relaxivity of O_2 by 40% on average. This over-estimation of relaxation is independent of the two methods of treating ε in the analysis of CW power saturation. Furthermore, both the oxygenated and deoxygenated data in Tables 2 and 4 shows that the individual products $R_1 \cdot R_2$ formed from the TD measured R_1 and CW estimated R_2 are systematically less than the value of P_2. Two possible reasons can be conjectured for this trend. First, the linewidth estimated R_2^0 value may not be the entire contribution to the spin-spin relaxation rate found in P_2. A study in which simulated spectra were fit to the "rollover" equation within the intermediate motion regime, based upon a stochastic Liouville equation approach, showed that the effective R_2 component of P_2 (from fits of the simulated data to Eq. (1)) obtained values that exceeded the measured linewidth within the ns to μs correlation time range [41]. Second, when the CW spectrum represents a composite of dynamics, the measured peak-to-peak linewidth (from which R_2 is estimated) may capture only the effects of the faster dynamics. Rapid dynamics are over emphasized in the linear CW peak-to-peak maxima in comparison to broader slower motion components associated with larger R_2 relaxation rates. This means that the measured peak-to-peak linewidth, at low microwave power, may not reflect the presence of larger R_2 components that contribute to the power saturation profile (and therefore the value of P_2) at higher microwave powers. The P_2 parameter, as it is derived from CW spectra in both the linear and saturated regimes, may reflect the presence of these larger R_2 contributions that are not cancelled by the low power estimate obtained from the peak-to-peak linewidth. The results for hGIIA $sPLA_2$ enzyme bound to vesicles (Fig. 12, right panel) show better agreement in scaling between the CW and TD measured relaxivities. The CW first harmonic in-phase absorption spectra were visibly slowed in comparison to the absence of membrane substrate binding (see Table 2 column 3 vs. Table 3 column 3). The steric restriction of spin-label motion upon binding to vesicles resulted in a loss of faster motion components in the CW spectrum, and resulted in peak-to-peak linewidths that were larger on average by a factor of 2. The larger linewidths were more inclusive of the total composition of spin-label dynamics. Fig. 12 illustrates that in general the peak-to-peak linewidth does not accurately remove all of the R_2^0 dependence from ΔP_2. Use of the peak-to-peak linewidth systematically underestimates R_2^0 dependence of ΔP_2.

Fig. 13 shows the data from Fig. 12 represented as an exposure factor (Eq. (4)). The CW ΔP_2 ratios are presented with and without correction by the linewidth for comparison (right and left panels respectively). The exposure factors from ΔP_2's are plotted vs. the exposure factors from ΔR_1's. Neither of the CW measured exposures is completely satisfactory in reproducing the TD values. There are two clusters of data points visible in both the right and left panels (113, 63, 56, 70 and 120, 19, 115, 3). This trend is inherited from the numerator of the exposure factor (see Fig. 12, right panel). The ratio represented by the exposure factor puts a high demand upon the CW data, in that the R_2 dependence must first be correctly reflected in P_2 without tradeoff from ε, and must, furthermore, be cancelled by the linewidth. In practice, such a direct exposure factor has not been used in the context of O_2 exposure data, for just these reasons. The TD relaxation data does not have the aforementioned defects. It should be noted that even with perfect data the exposure ratio reflects two fundamentally separate contributions to relaxation; both the relaxivity, χ, and $[O_2]$ dependencies (Eqs. (3) and (4)). The relative diffusion of oxygen and spin label may be affected by binding to the membrane, and will result in different χ factors for the bound vs. unbound conditions. Thus, changes in the concentration of O_2 and χ upon binding are not necessarily resolved individually but are both reflected in Φ.

Both CW and TD measurements predict that the relaxation effect of O_2 ($\chi \cdot [O_2]$) is reduced upon binding of hGIIA $sPLA_2$ to vesicles, and is the main experimental conclusion to be drawn from Fig. 13. A similar reduction has been observed for oxygen collisional relaxation by pSR using spin-labeled-lipid-analogs at various depths of penetration into the membrane phase [17]. There is a marked reduction of $\chi \cdot [O_2]$ in the head group region. Recent CW power saturation data from Cafiso et al. show a similar reduction of the oxygen exposure for selected residues of the spin-labeled C2 domain of $cPLA_2$ on PS/PC LUV, which are also thought to be near the membrane surface [45]. Because the hGIIA $sPLA_2$ enzyme is bounded on multiple surfaces in the *vesicle system*, a general $\chi \cdot [O_2]$ reduction is seen for residues over the entire enzyme surface [34]. Additionally, the hGIIA enzyme exhibits reduced O_2 exposure

when bound to *mixed micelles* (see Table 2 columns 4, 7, 8, and 9). The values of $\chi \cdot [O_2]$ deduced from R_1 pSR measurements range between 15 and 80% of their values in the absence of micellular dispersion (Table 2). To test relaxation by oxygen in the aqueous component of the micellular dispersion, the relaxation of the hydrophilic probe ^{14}N deuterated TEMPOL by O_2 was measured in the presence of micelles at the same concentration of detergent as used in the enzymatic study. The value of $\chi \cdot [O_2]$ was 73% of its value in the absence of micelles, and was deduced from R_2 measurements similar to those shown in Fig. 8 on each of the ^{14}N manifolds (data not shown). The use of aqueous relaxants (CROX and NiEDDA) with this micelle system did not show a depression in relaxation like that observed for O_2. If the translational diffusion in the aqueous component were affected by presence of the micelle detergent the relaxivity χ, because it depends on transport parameters, would be affected. The invariance of the relaxation from the aqueous relaxants CROX and NiEDDA argues that the transport component of relaxation, χ, is not affected but that in the oxygen relaxation, $\chi \cdot [O_2]$, the actual O_2 concentration in the aqueous phase is reduced. A similar reduction in O_2 concentration is observed in glycerol solutions, for example [23,34].

To avoid the complications of the χ dependence of relaxation Hubbell and co-works have used a ratio of O_2 relaxation for enzyme bound to the membrane substrate (given by $\Delta P_2/R_2^0$) vs. the analogous value of $\Delta P_2/R_2^0$ for a neutral spin relaxant such as NiEDDA to gauge relative exposures of spin-labeled sites within and proximal to the membrane [11,45]. Because this ratio involves measurements only on the membrane bound species, the intrinsic R_2^0 components of the ΔP_2's are the same for the two relaxant measurements, and cancel in the ratio. Furthermore, because the transport properties of O_2 and NiEDDA are similar, the relaxivity factor, χ, is nearly cancelled. The ratio of these relaxation gradients has empirically been found to provide a monotonic scale which varies with depth of penetration into the membrane phase [11,77].

In another context, a ratio analogous to that in Fig. 13, left, has been defined for binding of soluble peripheral membrane proteins to charged membrane surfaces, using charged relaxants. The effect of the relaxing agent in solution with no membrane is compared with the effect when the protein is bound to the membrane surface in the presence of the same bulk concentration of relaxant. The modification of ΔP_2 is interpreted as being due to the electrostatic-induced gradient of relaxant near the membrane surface [10,46]. For spin-labeled sites located away from the protein-membrane binding site the dynamics of the spin-label (and so the R_2^0) remain dominated in the bound state by the local motion of the flexible linkage through which the spin label is attached to the protein. Expression of the exposure as a direct ratio of ΔP_2 values is therefore applicable.

Another example of the application of $\Delta P_2/R_2^0$, where the intrinsic R_2^0 dependence of P_2 remains constant, is the measurement presented in the results above, in which the local electrostatic potential on a protein is determined. The relaxation of a spin-label on a charged protein by a charged spin relaxant was measured as a function of solution ionic strength (NaCl concentration). Fig. 14 illustrates the interaction of spin-labeled enzyme hGIIA $sPLA_2$ with the charged relaxant CROX by presenting the central feature of the CW spectrum as a function of CROX concentration and NaCl concentration. The interaction is anomalously strong in comparison to neutral proteins under the same conditions (see Section 3). Fig. 15 shows how the electrostatic interaction of hGIIA $sPLA_2$ with CROX was quantified through the salt dependence of CROX relaxivity by both CW power saturation and pSR. The TD and CW results track well because there is no change in the motional dynamics of the spin-label for the different experimental conditions (the R_2^0 contribution to ΔP_2 is constant as a function of NaCl). The value of R_2^0 necessary to scale the CW ΔP_2 to the TD ΔR_1 was 25% larger than expected from the rough peak-to-peak linewidth measurement. This factor is analogous to the factor of similar magnitude found for oxygen relaxation ΔP_2 values, as discussed above (see Fig. 12, left and entries for N70 in Table 2). The results obtained by both CW and TD techniques fit well with a simple theory of salt dependent mediation of surface charge (see Section 3, Eq. (8)).

One possible CW method, to avoid the use of power saturation, would be to infer the relaxivity from the change in CW linewidth under linear microwave power. This can give a quantitative result, in as much as the linewidth reflects the R_2 relaxation rate. The broadening of the linewidth may be quantified by convolution of the experimental CW spectrum without relaxing agent by a Lorentizian lineshape of adjustable rate until optimal comparison with broadened experimental CW spectrum is achieved. The convolution method has been applied to oxygen relaxation of spin-labeled lipid analogs in membranes, for example [78]. For the data in Fig. 15 (0.5 mM CROX) the maximum change in relaxation rate, for low salt, was on the order of 200 mG, which is the lower limit of linewidth change measured by the convolution technique in the cited study. The convolution technique, applied with appropriate concentration of relaxant is a reasonable alternative if a pulsed spectrometer is unavailable, or if CW spectra are acquired on a spectrometer with insufficient microwave power to obtain a full CW power saturation curve.

We used an alternative TD method to measure the electrostatic potential of the surface of the hGIIA $sPLA_2$ enzyme: The surface potential of was measured

using ^{14}N–^{15}N TD collisional relaxation (see Section 3). The charged and neutral ^{15}N nitroxides employed act as relaxants of the ^{14}N spin-labeled protein. The ^{15}N nitroxide resonance positions do not overlap significantly with the central feature of the ^{14}N spin-labeled protein. However, a contamination of the ^{15}N probe with ^{14}N at the 1% level can potentially interfere with these measurements if the relative concentration between relaxant and protein approaches a factor of 100. Furthermore, a small contribution to the pSR signal is always present between the two ^{15}N lines due to FID-like beating between the two frequency positions. For all measurements described here a background of the 1% level ^{14}N contaminant of the ^{15}N nitroxide relaxant was acquired in the absence of protein to assess its significance, and was found to provide a negligible contribution. The technique of CW ELDOR may be used to make similar measurements by CW methods, and has been applied to the measurement of the surface potential of DNA (with [DNA]/[relaxant] ≈ 0.5) [50]. pSR offers both the frequency selectivity of the CW ELDOR technique, as well as timescale separation. Surface potential measurements by ^{14}N–^{15}N cross-relaxation have the advantage that the ionic strength is constant for the experiments, as opposed to the salting experiments described above with CROX for which the surface potential must be modeled as a function of ionic strength at several salt concentrations.

The approximately +25 mV surface potential observed by the three methods described above was seen to have a most dramatic effect on CROX relaxation. The Boltzmann energy of a −1 charged species in the presence of this potential is only of the order of kT. However, −3 nominal charge on CROX, amplifies the protein–CROX interaction exponentially (Eq. (8)). The presence of even +25 mV protein surface charge presents a potential complication for applications using CROX as an intended probe of membrane electrostatics alone in protein-membrane binding studies. Previous studies have used neutral enzymes, and have relied upon the superposition of weak protein electrostatics with stronger membrane electrostatic forces [10,46].

4.3. In summary

Given the potential complications arising in the application of CW power saturation, TD pSR measurements appear as an attractive alternative. The consistency of CW power saturation data analysis can be improved in collisional relaxation studies by restricting the ε fitting parameter to be a common variable between the conditions with and without relaxant. Cancellation of the spin-spin relaxation rate dependence of ΔP_2 is only partially achieved by dividing by the experimental linear CW peak-to-peak linewidth. The peak-to-peak linewidth was observed to underestimate the R_2^0 component of ΔP_2. The relative values of ΔP_2's are quite reliable when used under conditions where the R_2^0 component is known to be constant.

4.4. Slow motion

Molecular correlation times in excess of 0.1 μs are characteristic of the slow motion X-band EPR regime. Powder pattern features appear in the linear first harmonic absorption spectrum for spin labels undergoing slow motion. Direct simulation of X-band CW spectra is possible, when a model of molecular motion is assumed [35,79]. Additionally, the CW technique of saturation transfer (ST-EPR), which becomes possible above 1 μs correlation time, can provide both structural and dynamic information [80,81]. The data presented here, for spin-labeled double stranded DNA, illustrate how the CW power-saturation method may be applied in the slow motion regime, and show the viability of TD oxygen collisional relaxation measurements. The conventional spectral measure used in the application of CW power-saturation is the peak-to-peak height of the first harmonic in-phase absorption spectrum. Fig. 16, left panel shows how this spectral feature (labeled A), ceases to retain its simple structure as motion slows (top vs. bottom spectra). The right panel gives an example of a spin-labeled DNA 28-mer fragment, and illustrates how the central peak-to-peak feature splits and becomes ambiguous in this regime of interest. To apply Eq. (1) to the analysis of the saturation behavior a new spectral feature that retains its shape within the slow motion regime must be chosen. The feature labeled "B" in Fig. 16, left panel, had been proposed based upon a theoretical study of simulated spectra in the slow motion regime [41]. The spin–lattice relaxation rates for the spin-labeled DNA from pSR are given in the legend. These may be compared with the rates found for a model nitroxide, as given in Fig. 10. The correlation times assigned to the DNA samples in Fig. 16 are for the end-over-end global tumbling mode of a rigid cylinder. Rotation about the DNA helical axis has a correlation time that is approximately 5 times faster than the end-over-end tumbling correlation time, but has a small influence because the principle axis of the spin-label is nearly aligned with the DNA helix axis. Furthermore, because of the rigid incorporation of the spin-label into the DNA backbone the internal collective torsional and flexural modes of motion of the DNA influence the relaxation rate. The time scale of these internal motions is on the order of 10 ns (see figure 7 of [35]). The magnitude of the relaxation rates observed in Fig. 16, when compared with the a model nitroxide at known correlation times (Fig. 10, top), argue that the internal modes of the DNA have a strong influence on the spin–lattice relaxation rate. The relaxation rates given in the legend of Fig. 16 were measured at equivalent microwave field

positions within the center and low field nuclear manifolds. The R_1 rate obtained was not dependent on which nuclear manifold was observed. This reflects the general manifold independence of the spin–lattice relaxation rate for nitroxides, which has been confirmed for fast motion theory and experiment [65,82]. No strong intra-manifold dependence of R_1 was observed for the DNA samples in Fig. 16. A weak intra-manifold dependence of R_1, however, becomes relevant in the 1 μs correlation-time range and represents intra-manifold saturation transfer [83]. A strong intra-manifold/nitroxide-orientational dependence of R_1 has been observed in low temperature glassy solvents [84]. Dominance of the faster internal modes of the DNA, as an R_1 relaxation mechanism, over the global tumbling modes of the DNA is a possible explanation for the intra-manifold insensitive rates observed here because the saturation transfer rate would be too fast to observe [83]. The effect of the SHF structure on the TD spectra, as would be seen through the FID-type component of pSR, is not evident because the R_2 rate exceeds the R_1 rate by two orders of magnitude in the slow motion regime.

Fig. 17 shows an experimental application of the CW power saturation method to the low field feature on an ^{15}N spin-labeled 50-mer duplex DNA. In addition, a pulsed saturation recovery measurement of the spin–lattice relaxation rate was made, and was observed to be nuclear-manifold independent. The value of R_2 predicted by P_2/R_1 is 30% larger than the intrinsic R_2^0 obtained from fitting the low temperature CW powder pattern spectrum (see Section 3) [35]. A value of R_2 that is larger than the value obtained in the powder pattern limit is consistent with the presence of both local flexural and global DNA dynamics (see discussion of Fig. 16 above).

Because the power saturation method applied to the low field feature measures a peak height above baseline, in order to successfully obtain CW power saturation data on the low field feature, the quality of the spectral baseline must hold up under the higher microwave powers. R_2 is decreasing as a function of increasing correlation time in the slow motion regime (note the spectral sharpening in Fig. 16, right panel as motion slows). R_1 is also decreasing with increasing correlation time (it continues as in Fig. 10, top). This means that the P_2 value is decreasing as a function of correlation time in the slow motion regime, and consequently the low field spectral feature is easily saturated. The high microwave powers that tend to distort baselines are not necessary to obtain an adequate "rollover" curve under slow motion conditions. However, when collisional relaxation by a paramagnetic species is introduced, higher powers become necessary to properly saturate and obtain a "rollover" curve and baseline quality could be a concern. Pulsed saturation recovery pSR is attractive as an alternative.

Fig. 18 exhibits the motional dependence of R_1 for spin-labeled 50-mer duplex DNA at several temperatures, with and without 50% sucrose. The correlation times used in this figure are the global end-over-end tumbling correlation times of the DNA. However, R_1 is influenced by a mixture of internal and global uniform modes of motion (see discussion of Fig. 16). The main potential complication for pSR measurements in the slow motion regime is the emergence of the spin-nuclear relaxation rate as a competitive component. The middle panel shows the pSR spectra for the 50-mer DNA at 20 °C at two sucrose concentrations, and demonstrates how the pSR spectrum is clearly bi-exponential. The bottom panel shows the relative magnitude of the second rate containing R_{1n}, as a function of motion. The order of magnitude difference exhibited between this second rate and R_1 shows that the spin-nuclear rate does not seriously interfere with the determination of R_1.

The pSR spectrum of 50-mer DNA in the presence and absence of O_2 is shown in Fig. 19. The increase in R_1 of the nitroxide through collisional relaxation with O_2 (given by the ΔR_1 difference) for the DNA is smaller than that obtained for a small nitroxide in aqueous solution at the same temperature (see Fig. 7 and discussion). This is due to the decreased diffusive mobility of the DNA-bound nitroxide probe and the fact that the DNA obstructs roughly half of the angular exposure of the spin-label to oxygen.

5. Conclusions

We have compared CW power saturation methods with TD pSR for the determination of relaxation rates over motional timescales that span fast motional to slow motional dynamics. For sub-nanosecond motional timescales, the SHF structure plays a decisive role in the proper analysis of both CW and TD signals. SHF contributions to CW signals have been well studied. Here, however, we have fit model predictions by global analysis to a larger set of the possible CW signals than has previously ever been described. The set tested in this paper includes all signals at the first and second harmonic of the Zeeman modulation, and includes spectra that were acquired with saturating microwave powers. All signals at each microwave power were acquired synchronously, using our novel Fourier-transform spectrometer, so that absorption/dispersion and Zeeman phase settings were truly acquired under the same conditions. Two distinct models of the SHF structure of TEMPOL were explored, with the conclusion that the microwave power dependence of the conventional CW absorption first harmonic in-phase signal, alone, was not sufficient to discriminate between the two models. The better fitting model predicted a spin–spin relaxation rate that was a factor of two smaller than the poorer fitting

model. The presence of SHF structure was found to corrupt the commonly applied analysis of power saturation using Eq. (1). A single ε factor failed to account for the curvature of the "rollover" curve and the fitted P_2 parameter was about 20% lower than the known value in the example shown. It was seen that over-modulation of the absorption signal does not suppress the influence of SHF structure. In fact, over-modulation was found to introduce further disagreement between the underlying relaxation rates and the prediction of the fit parameter P_2. The model of SHF structure obtained from detailed CW fitting assisted in the analysis of the pSR spectrum and FID of the protonated TEMPOL nitroxide. Both experiment and theoretical simulation using the Bloch equations showed that the pSR signals have a dependence on the SHF structure. The effective spin–lattice relaxation rate, obtained by a fit of the long-time pSR decay to a single exponential, was investigated as a function of pulse width. The effective relaxation rate dramatically varied with pulse width as the pulse width passed through the first major SHF envelope. These results confirm that the long-pulse limit gives the most accurate estimate of the spin–lattice relaxation rate when resolved SHF structure is present. In contrast, FID spectra acquired using short pulses on deuterated TEMPOL showed that when the SHF structure is present but is not well resolved, rates can be disentangled from the SHF envelope. pSR measurements on the spin-labeled protein hGIIA $sPLA_2$, and spin-labeled DNA were presented, because (1) their concentrations and complexity are typical of real applications, and (2) they represent examples whose structural and dynamic properties are typically studied by CW techniques. Two advantages of pSR over CW power saturation were apparent. First, the spin–lattice relaxation rate was measured without any change in methodology over a wide range of molecular motion, moreover the dependence of the spin–lattice relaxation rates on molecular motion was simple. The CW power saturation technique, in contrast, involved qualitatively complex changes in lineshape across the correlation times studied, and necessitated a change in the experimental spectral parameter used for analysis in specific motional regimes. While simple CW spectral parameters (such as the experimental linewidth) exhibited the same sensitivity to dynamics as the spin–lattice relaxation rate, again, no single CW measurement could be generalized to the entire range of correlation times. Second, the pSR measurement isolates the effect of collisonal relaxation to a single rate R_1. Accurate determination of the shift in the R_1 relaxation rate is the basis for structural investigations using collisional relaxation. To use the CW power saturation parameter P_2 directly as a measure of collisional relaxation, an independent estimate of the rate R_2^0, from the linewidth, was necessary. Comparison of collisional relaxation rates from TD with the CW estimates indicated that the linewidth did not remove all R_2 dependence from P_2 consistently. In cases where R_2^0 does not change significantly (such as when local relaxant concentration is changed electrostatically by adding salt) an independent estimate of R_2^0 is not needed and P_2 may be used directly to obtain structural information. However, in general there is no well-established methodology to extract an accurate R_1 from CW progressive saturation experiments. Furthermore, unlike pSR fitting, the reliance of the CW measurement upon a further adjustable parameter (ε) introduced uncertainty in extracting the P_2 relaxation parameter. We chose a test case that reflected the true conditions in which the CW technique of power saturation is commonly applied; namely, a spin-label, attached to a protein, that exhibits a range of dynamics. We investigated common methods to make the CW technique give self-consistent values for the relaxation parameters, and we find that no CW method provides absolute consistency when compared to the relaxation parameters measured independently by TD pSR. While the consistency of the CW power saturation parameter P_2 among data sets with common R_2 relaxation rates allows for improved accuracy of the CW technique, no analogous restriction is necessary with the TD pSR measurements.

Acknowledgments

This work was supported by Grants HL36235, HL50040, and GM065944 from the National Institutes of Health and UW Environmental Sciences Center Grant P30-ESO7033 from NIEHS. We thank Dr. Tamara Okonogi for help in DNA preparation and purification.

References

[1] C. Altenbach, S.L. Flitsch, H.G. Khorana, W.L. Hubbell, Biochemistry 28 (1989) 7806–7812.
[2] W.L. Hubbell, D.S. Cafiso, C. Altenbach, Nat. Struct. Biol. 7 (2000) 735–739.
[3] C. Altenbach, T. Marti, H.G. Khorana, W.L. Hubbell, Science 248 (1990) 1088–1092.
[4] T.C. Miller, S.C. Alley, A.W. Reese, M.S. Solomon, W.V. McCallister, C. Mailer, B.H. Robinson, P.B. Hopkins, J. Am. Chem. Soc. 117 (1995) 9377–9378.
[5] T.M. Okonogi, S.C. Alley, A.W. Reese, P.B. Hopkins, B.H. Robinson, Biophys. J. 78 (2000) 2560–2571.
[6] T.E. Edwards, T.M. Okonogi, B.H. Robinson, S.T. Sigurdsson, J. Am. Chem. Soc. 123 (2001) 1527–1528.
[7] E.V. Bobst, R.S. Keyes, Y.Y. Cao, A.M. Bobst, Biochemistry 35 (1996) 9309–9313.
[8] P.Z. Qin, S.E. Butcher, J. Feigon, W.L. Hubbell, Biochemistry 40 (2001) 6929–6936.
[9] A.H. Beth, R. Wilder, L.S. Wilkerson, R.C. Perkins, B.P. Meriwether, L.R. Dalton, C.R. Park, J.H. Park, J. Chem. Phys. 71 (1979) 2074–2082.

[10] Y. Lin, R. Nielsen, D. Murray, W.L. Hubbell, C. Mailer, B.H. Robinson, M.H. Gelb, Science 279 (1998) 1925–1929.
[11] C. Altenbach, D.A. Greenhalgh, H.G. Khorana, W.L. Hubbell, Proc. Natl. Acad. Sci. USA 91 (1994) 1667–1671.
[12] J.H. Freed, G.K. Fraenkel, J. Chem. Phys. 39 (1963) 326–348.
[13] B.H. Robinson, D.A. Haas, C. Mailer, Science 263 (1994) 490–493.
[14] J.S. Hyde, in: L. Kevan, R.N. Schwartz (Eds.), Time Domain Electron Spin Resonance, Wiley-Interscience, 1979, pp. 1–30.
[15] M. Huisjen, J.S. Hyde, Rev. Sci. Instrum. 45 (1974) 669–675.
[16] W. Froncisz, J.S. Hyde, J. Magn. Reson. 47 (1982) 515–521.
[17] W.K. Subczynski, J.S. Hyde, A. Kusumi, Proc. Natl. Acad. Sci. USA 86 (1989) 4474–4478.
[18] J.S. Hyde, J.J. Yin, J.B. Feix, W.L. Hubbell, Pure Appl. Chem. 62 (1990) 255–260.
[19] C. Altenbach, W. Froncisz, J.S. Hyde, W.L. Hubbell, Biophys. J. 56 (1989) 1183–1191.
[20] C. Altenbach, W. Froncisz, W.L. Hubbell, in: Biophysical Society 46th Annual Meeting vol. 82, pp. 479a, 1 vols., Biophysical Journal, San Francisco, CA, 2002.
[21] R. Nielsen, S. Cannan, F. Ghomashchi, M.H. Gelb, B.H. Robinson, in: Biophysical Society 46th Annual Meeting vol. 82, pp. 480a, 1 vols., Biophysical Journal, San Francisco, CA, 2002.
[22] P.W. Percival, J.S. Hyde, J. Magn. Reson. 23 (1976) 249–257.
[23] B.H. Robinson, C. Mailer, A.W. Reese, J. Magn. Reson. 138 (1999) 210–219.
[24] J.J. Windle, J. Magn. Reson. 45 (1981) 432–439.
[25] T. Oles, R.A. Strangeway, J. Luglio, W. Froncisz, J.S. Hyde, Rev. Sci. Instrum. 63 (1992) 4010–4011.
[26] Applied Precision Inc.
[27] P.B. Kingsley, J. Magn. Reson. A 110 (1994) 102–105.
[28] J.S. Hyde, W. Froncisz, J. Magn. Reson. 47 (1982) 515–521.
[29] Molecular Specialties Inc., Milwaukee, WI.
[30] C.P. Poole, Electron Spin Resonance: A Comprehensive Treatise on Experimental Techniques, Wiley, New York, 1983.
[31] T. Sasaki, Y. Kanaoka, T. Watanabe, S. Fujiwara, J. Magn. Reson. 38 (1980) 385–390.
[32] Y. Shimoyama, H. Watari, Appl. Spectrosc. 43 (1989) 1021–1026.
[33] W. Froncisz, T.G. Camenisch, J.J. Ratke, J.S. Hyde, Rev. Sci. Instrum. 72 (2001) 1837–1842.
[34] S. Canaan, R. Nielsen, F. Ghomashchi, M.H. Gelb, B.H. Robinson, J. Biol. Chem. 277 (2002) 30984–30990.
[35] T.M. Okonogi, A.W. Reese, S.C. Alley, P.B. Hopkins, B.H. Robinson, Biophys. J. 77 (1999) 3256–3276.
[36] B.H. Robinson, J. Chem. Phys. 78 (1983) 2268–2273.
[37] B.H. Robinson, C. Mailer, A.W. Reese, J. Magn. Reson. 138 (1999) 199–209.
[38] F.P. Auteri, A.H. Beth, B.H. Robinson, J. Magn. Reson. 80 (1988) 493–501.
[39] T. Sugano, C. Mailer, B.H. Robinson, J. Chem. Phys. 87 (1987) 2478.
[40] C. Mailer, D.A. Haas, E.J. Hustedt, J.G. Gladden, B.H. Robinson, J. Magn. Reson. 91 (1991) 475–496.
[41] D.A. Haas, C. Mailer, B.H. Robinson, Biophys. J. 64 (1993) 594–604.
[42] J.S. Hyde, W.K. Subczynski, in: L.J. Berliner, J. Reuben (Eds.), Biological Magnetic Resonance: Spin Labeling Theory and Applications, vol. 8, Plenum, New York, 1989, pp. 399–425.
[43] E.J. Hustedt, H. Thomann, B.H. Robinson, J. Chem. Phys. 92 (1990) 978–995.
[44] B.L. Bales, in: L.J. Berliner, J. Reuben (Eds.), Biological Magnetic Resonance: Spin Labeling Theory and Applications, vol. 8, Plenum, New York, 1989, pp. 77–126.
[45] A.A. Frazier, M.A. Wisner, N.J. Malmberg, K.G. Victor, G.E. Fanucci, E.A. Nalefski, J.J. Falke, D.S. Cafiso, Biochemistry 41 (2002) 6282–6292.
[46] A. Ball, R. Nielsen, M.H. Gelb, B.H. Robinson, Proc. Natl. Acad. Sci. USA 96 (1999) 6637–6642.
[47] Y. Lin, F. Ghomashchi, R. Nielsen, Y. Snitko, B.Z. Yu, S.K. Han, W. Cho, D.C. Wilton, M.K. Jain, B.H. Robinson, M.H. Gelb, Biochem. Soc. Trans. 26 (1998) 341–345.
[48] N. Lakshminarayanaiah, Equations of Membrane Biophysics, Academic Press, New York, 1984.
[49] J.-J. Yin, J.S. Hyde, J. Magn. Reson. 74 (1987) 82–93.
[50] Y.K. Shin, W.L. Hubbell, Biophys. J. 61 (1992) 1443–1453.
[51] T.M. Okonogi, S.C. Alley, E.A. Harwood, P.B. Hopkins, B.H. Robinson, Proc. Natl. Acad. Sci. USA 99 (2002) 4156–4160.
[52] B.H. Robinson, C. Mailer, G. Drobny, Annu. Rev. Biophys. Biomol. Struct. 26 (1997) 629–658.
[53] K.M. More, G.R. Eaton, S.S. Eaton, J. Magn. Reson. 60 (1984) 54–65.
[54] V.A. Livshits, T. Pali, D. Marsh, J. Magn. Reson. 133 (1998) 79–91.
[55] M.P. Eastman, R.G. Kooser, M.R. Das, J.H. Freed, J. Chem. Phys. 51 (1969) 2690–2790.
[56] B.H. Robinson, L.R. Dalton, Chem. Phys. 36 (1979) 208–237.
[57] J.R. Taylor, An Introduction to Error Analysis, Oxford University Press, Oxford, 1982.
[58] S.A. Goldman, G.V. Bruno, C.F. Polnaszek, J.H. Freed, J. Chem. Phys. 56 (1972) 716–735.
[59] L.J. Berliner, in: L.J. Berliner (Ed.), Spin Labeling Theory and Applications, vol. 1, Academic Press, New York, 1976, pp. 53–132.
[60] R. Nielsen, B.H. Robinson, A.H. Beth, E.J. Hustedt, in: 45th Rocky Mountain Conference on Analytical Chemistry: EPR, Denver, Co., 2003.
[61] R. Nielsen, in: Chemistry, University of Washington, Seattle, 2003, pp. 1–409.
[62] W.S. Warren, J. Chem. Phys. 81 (1984) 5437–5448.
[63] L.J. Schwartz, A.E. Stillman, J.H. Freed, J. Chem. Phys. 77 (1982) 5410–5425.
[64] R.N. Schwartz, L.L. Jones, M.K. Bowman, J. Phys. Chem. 83 (1979) 3429–3434.
[65] B.H. Robinson, A.W. Reese, E. Gibbons, C. Mailer, J. Phys. Chem. B 103 (1999) 5881–5894.
[66] P.W. Atkins, K.A. McLauchlan, P.W. Percival, Mol. Phys. 25 (1973) 281–296.
[67] W.K. Subczynski, J.S. Hyde, A. Kusumi, Biochemistry 30 (1991) 8578–8590.
[68] T.I. Smirnova, A.I. Smirnov, R.B. Clarkson, R.L. Belford, Magn. Reson. Med. 33 (1995) 801–810.
[69] J.R. Harbridge, S.S. Eaton, G.R. Eaton, J. Magn. Reson. 159 (2002) 195–206.
[70] Y. Zhou, B.E. Bowler, G.R. Eaton, S.S. Eaton, J. Magn. Reson. 139 (1999) 165–174.
[71] J.H. Freed, G.V. Bruno, C.F. Polnaszek, J. Phys. Chem. 75 (1971) 3385–3399.
[72] S.A. Goldman, G.V. Bruno, J.H. Freed, J. Chem. Phys. 59 (1973) 3071–3091.
[73] D.J. Schneider, J.H. Freed, in: J.O. Hirschfelder, R.E. Wyatt, R.D. Coalson (Eds.), Lasers, Molecules and Methods, Wiley, New York, 1989, pp. 387–527.
[74] L. Columbus, W.L. Hubbell, Trends Biochem. Sci. 27 (2002) 288–295.
[75] C.A. Popp, J.S. Hyde, J. Magn. Reson. 43 (1981) 249–258.
[76] W.K. Subczynski, J.S. Hyde, Biochim. Biophys. Acta 643 (1981) 283–291.
[77] G.E. Fanucci, N. Cadieux, C.A. Piedmont, R.J. Kadner, D.S. Cafiso, Biochemistry 41 (2002) 11543–11551.
[78] A.I. Smirnov, R.B. Clarkson, R.L. Belford, J. Magn. Reson. B 111 (1996) 149–157.

[79] J.H. Freed, in: L.J. Berliner (Ed.), Spin Labeling Theory and Applications, vol. 1, Academic Press, New York, 1976, pp. 53–132.
[80] E.J. Hustedt, A.I. Smirnov, C.F. Laub, C.E. Cobb, A.H. Beth, Biophys. J. 72 (1997) 1861–1877.
[81] E.J. Hustedt, A.H. Beth, Biophys. J. 81 (2001) 3156–3165.
[82] J.J. Yin, J.B. Feix, J.S. Hyde, Biophys. J. 52 (1987) 1031–1038.
[83] D.A. Haas, T. Sugano, C. Mailer, B.H. Robinson, J. Phys. Chem. 97 (1993) 2914–2921.
[84] J.-J. Du, G.R. Eaton, S.S. Eaton, J. Magn. Reson., Ser. A 115 (1995) 213–221.